



Project Deliverable

Grant Agreement number	308952
Project acronym	OMSOP
Project title	OPTIMISED MICROTURBINE SOLAR POWER SYSTEM
Funding Scheme	FP7-ENERGY.2012.2.5.1:RESEARCH, DEVELOPMENT AND TESTING OF SOLAR DISH SYSTEMS
Work Package	WP1 – SYSTEM COMPONENT DEVELOPMENT
Deliverable number - title	D1.5 OPTIMIZED DISH DESIGN
Lead Beneficiary	INNOVA
Dissemination level	PU
Delivery month	JANUARY 2013
Name, title and organisation of the scientific representative of the project's coordinator	<p>Prof. Abdulnaser Sayma Professor of Energy Engineering City University London</p> <p>Tel: +44 (0)20 7040 8277 E-mail: a.sayma@city.ac.uk Project website address: www.omsop.eu</p>

Authors: Tommaso Crescenzi (ENEA), Michela Lanchi (ENEA), Valeria Russo (ENEA), Adio Miliuzzi (ENEA), Marco Montecchi (ENEA), Enzo Pastorelli (Innova), Alessandro Mariani (Innova)

Contents

Introduction	3
Stand-alone dish array: a feasibility analysis	4
Dish shape optimization and performance analysis	8
Dish shape optimization	8
<i>Geometrical aspects</i>	8
<i>Optics of the parabolic dish concentrator</i>	9
<i>Efficiency evaluation</i>	16
<i>Application of the “ray tracing” method</i>	21
<i>Conclusions</i>	28
Performance analysis	29
<i>Dimensions of the Innova PDC</i>	29
<i>Focal plane flux distribution using a ray-tracing method</i>	30
<i>Efficiency evaluation</i>	32
<i>Conclusions</i>	38
SIMUL-DISH: a portable ray tracing software for analytical dish simulation	40
Software description	40
Comparison between single and daisy-arrangement of dishes	44
Simulation according to the latest OMSoP project outlining	48
Wind loads analysis	50
Codes and Standards	50
Definition of the wind actions	50
Aerodynamic coefficients: CNR-DT207/2008	51
Aerodynamic coefficients: Wind tunnel experimental tests	54
Aerodynamic coefficients: methods comparison	60
Characterization of the ENEA Casaccia site	63
Evaluation of the peak forces and moments	64
Conclusions	64
Supporting structure	65
Tracking system specifications	69
References	71

Introduction

The main objective of the project is to develop and demonstrate advanced technical solutions for concentrated solar power systems (CSP) coupled to micro-gas turbine (MGT) to produce electricity in the range of 3-10 kW. The system is destined to fulfil energy needs for domestic and small commercial applications. The primary technical challenge is to enable the production of small scale cost effective, efficient and reliable units.

The parabolic dish concentrator technology, in particular, has to be improved in terms of concentration ratio increase and weight reduction. With this regard, the partners have considered different design solutions with the aim of increasing the dish performances maintaining a light and handy structure. Different dish configurations have been analysed, with a particular focus on two possible options: multi-dish arrangement, consisting of a structure composed of several dishes, or single dish configuration. In particular two possible configurations have been considered for the multi-dish arrangement: the “array” system, described and analysed in the paragraph “Stan-alone dish array: a feasibility analysis”, and the “daisy” structure, described and evaluated in the paragraph “SIMUL-DISH: a portable ray tracing software for analytical dish simulation”.

The selected dish arrangement has been successively tailored to the MGT-receiver requirements. In particular the solar collector has been optimized in terms of shape and materials for achieving the target concentration factor and turbine inlet temperature (~800°C). The optimization analysis and the dish performance evaluation have been reported in the paragraph “Dish shape optimization and performance analysis”.

Once defined the geometrical specifications of the dish, which will be realized and tested at Casaccia site, a wind load analysis has been carried out with the aim of evaluating the wind loads acting in realistic environmental conditions. The theoretical study and the results have been reported in the paragraph “Wind loads analysis”.

On the base of the dish geometrical specifications and calculated mechanical loads the supporting structure of the dish prototype has been defined along with the tracking system. Their description is reported in the paragraphs “Supporting structure” and “Tracking system specification”.

Stand-alone dish array: a feasibility analysis

(Tommaso Crescenzi, Michela Lanchi, Valeria Russo (ENEA))

In the frame of the Task1.2 “Dish arrangement design and optimization”, different dish configurations have been analysed, with a particular focus on the multi-dish arrangement, intended as a system composed of several dishes, with the aim of increasing the concentration factor and the turbine inlet temperature maintaining light and handy structures. In particular, two options have been investigated: the “daisy arrangement”, consisting in a concentrator structure composed of several dishes (4-6), and the “stand-alone dish array”, consisting in an array of separate dishes, each connected to a separate receiver. The analysis of the latter configuration is the object of the present paragraph.

The theoretical analysis has been performed assuming that all the dishes composing the array have the same concentration factor and that all the receivers are connected each other to provide the required thermal energy to a single Micro Gas Turbine (MGT), as shown in Figure 1.

As a first consideration, it is worth noticing that this option, with respect to the single dish configuration, implies a more expensive concentration system and a more extensive use of land.

Furthermore this layout leads to an efficiency reduction because of the relevant extension of the piping system required to connect the dish array unit to the MGT system. Indeed the piping network is composed of a principal header and several secondary lines (see Fig. 1) with inevitable thermal and mechanical energy losses, and consequently an overall efficiency reduction.

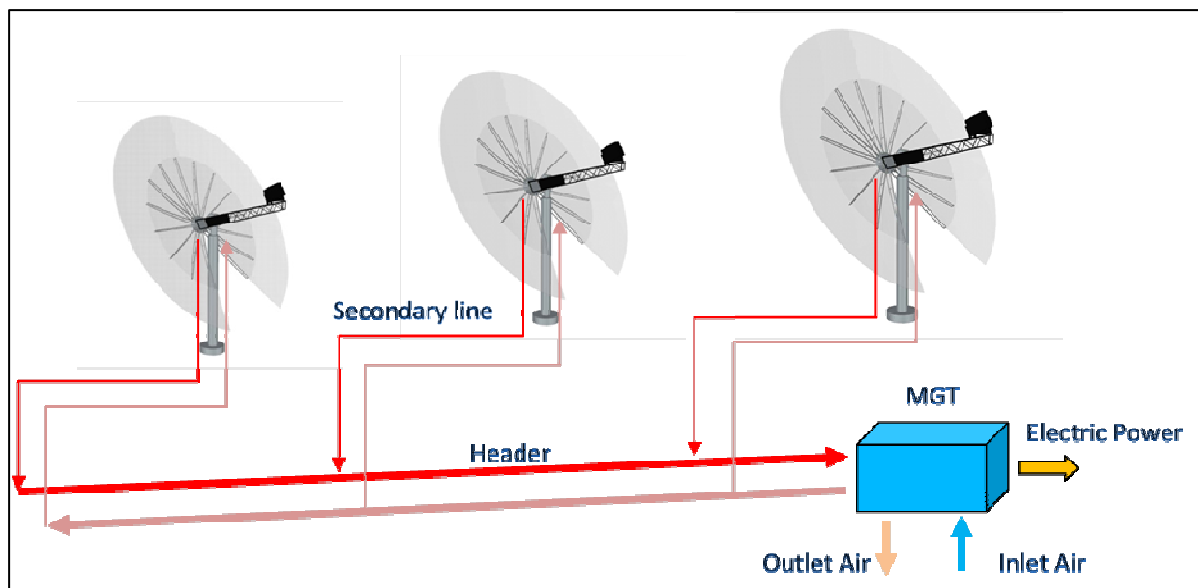


Figure 1 – Scheme of the stand-alone dish array concept

In order to compensate these losses and to maintain the same operation conditions at the inlet of the MGT it would be necessary to increase the outlet temperature of the receivers and the outlet pressure of the air compressor.

With the aim of evaluating the thermal and the mechanical energy losses related to the dish array option, a comparison between a single dish lay-out (60 m^2 of reflecting surface and 9 m of diameter) and a dish array configuration composed of 6 dishes (each characterized by 12 m^2 of reflecting surface and 4 m of diameter) has been carried out in terms of thermal performance.

The thermal efficiency of the dish-receiver system has been assumed equal to 50%, considering the optical efficiency of the dishes equal to 72% and the thermal efficiency of the receivers equal to 70%. Furthermore the concentration factor has been assumed to be constant in the two configurations, meaning that the receiver window in the dish array option is smaller than the single dish arrangement. With regard to the direct normal irradiation (DNI), a value of 900 W/m^2 has been assumed.

As for the MGT, represented in Figure 2, the following operative conditions have been assumed:

- Compressor outlet pressure (kPa) 320
- Turbine inlet temperature (°C) 750
- Air mass flow (kg/s) 0.1
- Compressor isentropic efficiency (%) 76
- Turbine isentropic efficiency (%) 80
- Recuperator efficiency (%) 90

The heat and mass balance calculation has been performed through the use of the GateCycle code, a commercial heat balance software for power plant simulation.

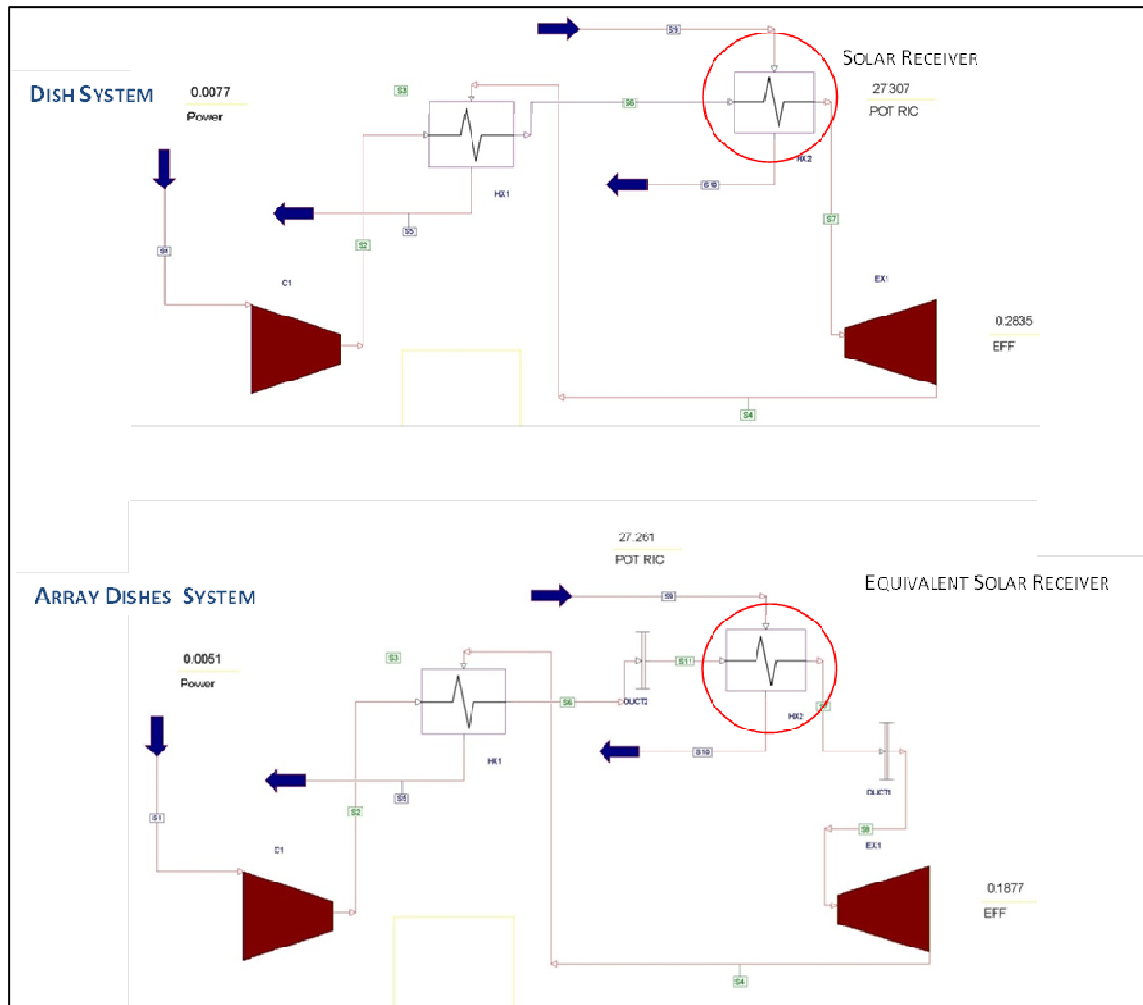


Figure 2 – Comparison between the single dish option and the stand-alone dish array configuration: process simulation through GateCycle code.

SINGLE DISH SYSTEM

Since the dish reflecting surface is 60 m^2 , and the dish-receiver system efficiency is 50%, the solar power collected is 54 kW_t , while the power available at the MGT inlet is about 27 kW_t . Considering the turbo alternator friction and the compression work, the turbine net electrical power is 7.7 kW_e , with a solar to electricity conversion efficiency of about 14%.

STAND-ALONE DISH ARRAY SYSTEM

As above mentioned the MGT unit is located outside the solar field, and connected to each receiver through a network of piping for the collection and distribution of the air flow. In analogy to what has been assumed for the single-dish system, the power available at each receiver window is 6.5 kW_t . ($54 \cdot 0.72 / 6 \text{ kW}_t$)

Regarding the piping system, it has been hypothesized that it is 30 m long and properly insulated. Therefore, assuming a linear thermal loss of about 150 W/m , the total power lost from the piping system can be estimated as 4.5 kW . Regarding the mechanical losses it has been assumed that the piping pressure drops represent a fixed percentage of the compressor outlet pressure (5% of 320 kPa).

On the base of these energy losses values, the heat and mass balance along the piping has been performed using the GateCycle simulation code. In particular the component "Duct" has been selected to simulate the behavior of the piping. The calculated temperature and pressure at the turbine inlet are 710°C and 287 kPa , respectively, while in the single-dish option they are 750°C and 320 kPa , respectively. In this case the power available at the MGT

inlet is 22.5 kW_t, while the net turbine electrical power is 5.1 kW_e, with a solar to electricity conversion efficiency of 9.4%. Therefore the thermal and mechanical energy losses have led to a reduction of about 34% of the net turbine electrical power with respect to the single dish case.

CONCLUSIONS

From the previous analysis it has clearly emerged that the use of the dish array configuration in place of the single dish option would significantly reduce the solar to electrical conversion efficiency of the system, increasing, at the same time, the investment costs.

Furthermore, with the aim of achieving the same operative conditions for the MGT unit (temperature and pressure) it would be necessary to increase the dishes surface and the pressure ratio of the compressor.

The single dish option which allows the physical integration between the receiver and the MGT unit is therefore more efficient and less expensive.

The adoption of the stand-alone dish array option is desirable only in view of a modular electricity production, with each dish equipped with its own receiver and MGT.

Dish shape optimization and performance analysis

(Adio Miliozzi (ENEA))

Dish shape optimization

As already mentioned in the introduction, the parabolic dish collector (PDC) system has to be coupled with a micro-gas-turbine (MGT) with electrical power (Pe) between 3 and 10 kW_e. The micro-gas-turbine should run with a receiver temperature of about 800-1000°C.

Assuming a maximum solar radiation (I) of about 800 W/m₂, a maximum global efficiency of about 25% (η_{tot}), and an utilization factor of the total area, f_{used} , of about 90%, we should get:

- A useful receiving surface: $S_{net} = Pe / (\eta_{tot} I) = 15 - 50 \text{ m}^2$;
- A total receiving surface: $S_{tot} = S_{net} / f_{used} = 16.7 - 55.6 \text{ m}^2$;
- An aperture diameter of the parabolic dish: $D = (4 \cdot S_{tot} / \pi)^{0.5} = 4.6 - 8.4 \text{ m}$

Consequently, the following analysis will be focused on parabolic dish concentrators having aperture diameters between **4 and 10 meters**, optimized to achieve a cavity receiver temperature of the order of **1000 °C**.

Geometrical aspects

The paraboloid is a revolution surface produced by an arc of parabola rotating around an axes passing from the vertex (parabolic dish). It is characterized by a focal distance F and a circular aperture area having diameter D .

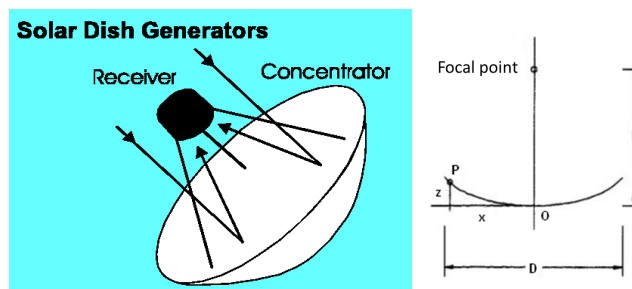


Figure 3- Paraboloid of revolution

The points of the paraboloid are defined by the equation: $x^2 + y^2 = 4F \cdot z$, or, in cylindrical

coordinates, by: $z = \frac{r^2}{4F}$

The surface area of the paraboloid may be found by integrating the previous equation over the appropriate limits. We can define a circular differential area strip on the paraboloid as shown in Figure 4 as

$$dA_s = 2\pi \cdot r \sqrt{dz^2 + dr^2}$$

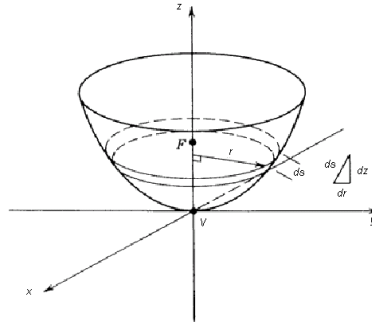


Figure 4- Parameters defining a circular strip of differential area.

Note that the differential element of arc ds is casted in terms of the height dz and the radial distance dr . Finding the derivative of z with respect to r , we express the differential area band as

$$dA_s = 2\pi \cdot r \cdot \sqrt{\left(\frac{r}{2F}\right)^2 + 1} \cdot dr$$

The full surface area A of a paraboloid having a focal length F and an aperture diameter D may be found by integrating the previous equation. The result is

$$A_s = \int_0^{D/2} dA_s = \frac{8\pi F^2}{3} \left\{ \left[\left(\frac{D}{4F}\right)^2 + 1 \right]^{3/2} - 1 \right\}$$

The concentrator aperture area A_a , of most importance for the prediction of the collected power, is simply the circular area defined by the aperture diameter D and is given by:

$$A_a = \frac{\pi}{4} D^2$$

A very important factor defining the geometry of a paraboloid is the F/D ratio, that is the ratio between the focal length and the diameter. Varying the parameter F/D leads to the modification of the parabola convexity. With the increase of the F/D ratio the parabola tends to be flatter, whereas with the F/D ratio reduction the parabola becomes more convex. In particular, if $F/D=0.25$, the focal point is located on the aperture plane of the paraboloid.

Optics of the parabolic dish concentrator

Solar imagine

A parabolic dish concentrator characterized by a diameter D and a focal distance F will be considered. The ratio between the focal distance and the concentrator diameter will be denoted by f :

$$f = \frac{F}{D}$$

Moreover, H is the extreme quote of the concentrator and $(F-H)$ the distance between the aperture plane and the focal plane (Figure 5).

$$H = \frac{R^2}{4F} = \frac{F}{16f^2} \quad F - H = \left(\frac{16f^2 - 1}{16f^2} \right) F$$

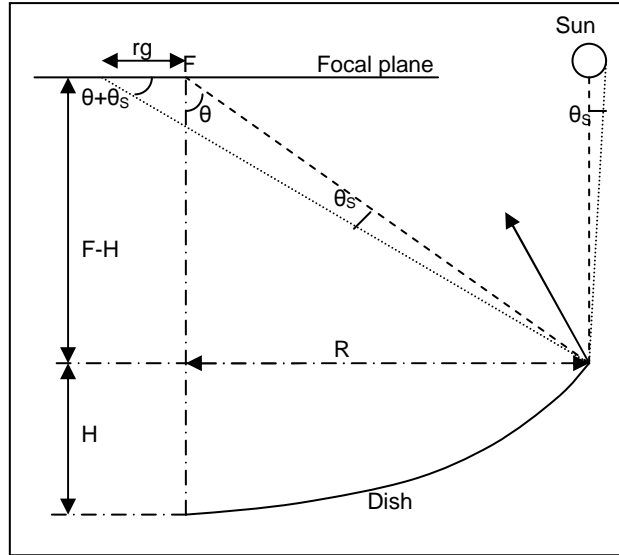


Figure 5- Schematic of concentrator reflection

The solar radiation falling on the parabolic concentrator is reflected, in the case of perfect reflection, to the focal point of the same. Indicating with θ the maximum angle between the reflected radiation and the normal to the focal plane one, the following relationship can be written:

$$\tan \theta = \frac{R}{F-H} = \frac{8f}{16f^2-1}$$

from which the value of the angle θ is derived as as a function of factor f:

$$\theta = \arctan\left(\frac{8f}{16f^2-1}\right)$$

Since the sun is seen from the earth with a half-opening angle θ_s , the reflected radiation does not affect in a point (the focus) but in a circular area of radius r_g located on the focal plane and said focal spot. In such a case the following relation holds:

$$\tan(\theta + \theta_s) = \frac{R+r_g}{F-H} = \tan(\theta) \left(1 + 2\frac{r_g}{D}\right)$$

from which it can be obtained the value of r_g in relation to the diameter D of the concentrator:

$$\frac{r_g}{D} = \frac{1}{2} \left(\frac{\tan(\theta + \theta_s)}{\tan(\theta)} - 1 \right)$$

This ratio is therefore a function of f and θ_s .

In general, the θ_s angle takes into account the natural section of the solar disk (4.7 mrad, 0.27°) increased by the contribution of the error on the shape of the mirrors, the imperfect specularity of the mirrors, the diffractions, the pointing errors and those concerning the alignment in the positioning of the mirrors and the receiver. Such errors are seen statistically independent so that the actual value of θ_s is the square root of the sum of the squares of the

individual errors. This value θ_s can be estimated equal to about 7-10 mrad (0.4°-0.57°) considering also the imperfections of the reflecting surface.

The concentration factor C of the focal spot will then have the following expression, function of the ratio between r_g and D:

$$C = \frac{\Phi_{mf}}{I} = \frac{1}{4(r_g / D)^2}$$

with Φ_{mf} the average irradiative flow on the focal spot and I the solar radiation.

If the ratio r_g/D is reported as a function of the shape factor f (Table 1 and Figure 6), it can be noted the presence of a minimum for **f=0.6**. The presence of this minimum indicates that, for a fixed diameter D, a F value exists, equal to 60% of the diameter, which minimizes the extension of the sunspot (r_g minimum) and, consequently, the aperture of the window of the receiver. Of course, in correspondence of this minimum, the concentration reaches its maximum which turns out to be, neglecting absorptions by the concentrator, equal to approximately 5000 suns.

In conclusion, it can be stated that the optimum values of f to minimize the size of the focal spot and to maximize the concentration of the solar flux are **between 0.55 and 0.7**, which corresponds to a θ angle between 49° and 39° and a concentration value exceeding 4900 suns.

f (-)	Tracking error		$\theta_s = 7 \text{ mrad}$		$\theta_s = 10 \text{ mrad}$	
	θ (rad)	θ (°)	r_g/D (-)	C (suns)	r_g/D (-)	C (suns)
0.30	1.39	79.61	0.02052	594	0.02982	281
0.35	1.24	71.08	0.01165	1843	0.01679	887
0.40	1.12	64.01	0.00902	3076	0.01296	1488
0.45	1.01	58.11	0.00789	4014	0.01133	1948
0.50	0.93	53.13	0.00736	4615	0.01056	2243
0.55	0.85	48.89	0.00712	4928	0.01021	2398
0.60	0.79	45.24	0.00705	5030	0.01010	2449
0.65	0.73	42.08	0.00708	4985	0.01014	2429
0.70	0.69	39.31	0.00718	4847	0.01029	2363
0.75	0.64	36.87	0.00733	4653	0.01050	2269
0.80	0.61	34.71	0.00751	4428	0.01076	2161
0.85	0.57	32.78	0.00772	4190	0.01106	2045
0.90	0.54	31.05	0.00795	3951	0.01138	1929
0.95	0.51	29.49	0.00820	3717	0.01174	1815
1.00	0.49	28.07	0.00846	3492	0.01211	1706
1.05	0.47	26.78	0.00873	3279	0.01249	1602
1.10	0.45	25.61	0.00901	3079	0.01289	1505
1.15	0.43	24.53	0.00930	2893	0.01330	1413
1.20	0.41	23.54	0.00959	2719	0.01372	1329
1.25	0.39	22.62	0.00989	2557	0.01414	1250
1.30	0.38	21.77	0.01019	2408	0.01457	1177

Table 1 – r_g/D ratio and C concentration factor as function of the shape factor f

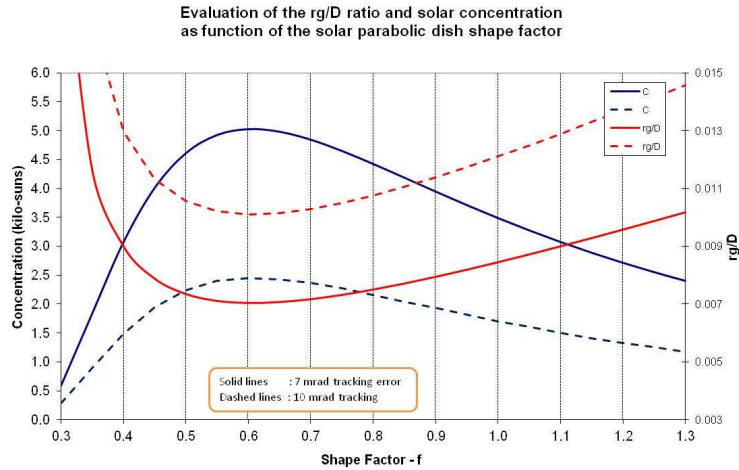


Figure 6- rg/D ratio and C concentration factor

Optimal shape factor

As stated in the previous paragraph, an optimal shape factor f to minimize the size of the focal spot and to maximize the concentration of solar flux must be chosen in the range **0.55-0.7**. The maximum concentration value (about 5000 suns) is obtained in correspondence of f equal to **0.6** but other considerations may lead to different choices. For example (see Figure 7), in correspondence of f equal to **0.7** the concentration factor is lower (about 4900 suns) but it is possible to reduce the reflecting area (less costs) and to increase the curvature radius (more flat surface and less technological problems).

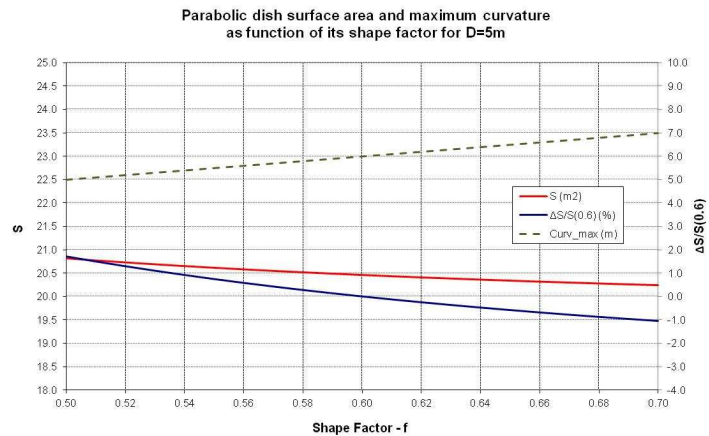


Figure 7 – Parabolic dish surface area and maximum curvature as a function of shape factor

However, at this stage, the maximization of the concentration factor is preferable compared to other considerations, also because the differences do not appear to be of great entity.

Solar flux distribution on the focal plane

In the previous solar image analysis, purely geometrical, it has not been considered that the distribution of the solar flux on the focal plane is not constant. Taking into account that the flow of the light source (sun) varies with the half angle θ_s and that the imperfections of the reflecting surface induce further distortions, the luminous flux on the focal plane may assume a Gaussian distribution (Figure 8) characterized by a peak flux Φ_{peak} and a standard deviation μ .

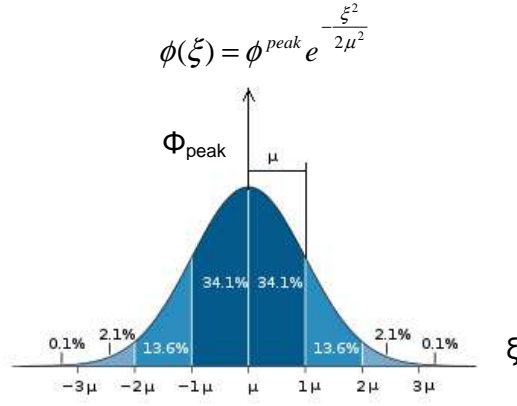


Figure 8 - Gaussian flux distribution

The incident power on a circular window centered on the focus of the parabolic concentrator with radius r is:

$$P(r) = \int_0^r 2\pi\xi\phi(\xi)d\xi$$

If $r = \infty$ then P_{in} is the total incident power on the focal plane.

$$P_{in} = P(\xi = \infty) = 2\pi\mu^2\phi^{peak}$$

Instead, having the window a finite radius r , P_w is the incident power on the receiver window

$$P_w = P(\xi = r) = 2\pi\mu^2\phi^{peak} \left(1 - e^{-\frac{r^2}{2\mu^2}} \right)$$

Since r_g is the radius of the window necessary to capture all the incident power while, in a Gaussian distribution, a window radius equal to 3 times the standard deviation corresponds to the 99% of intercepted power, it can be assumed the following equivalence:

$$r_g = 3\mu$$

Therefore, using the previous relations, we can identify the parameters describing the flow distribution in the focal plane, μ and Φ_{peak} :

$$\mu = r_g / 3$$

$$\phi^{peak} = \frac{P_{in}}{2\pi\mu^2} = \frac{\eta_c P_c}{2\pi\mu^2} = \frac{9}{8} \frac{\eta_c I}{(r_g / D)^2}$$

where η_c is the efficiency of the reflective surfaces (reflectance).

As shown, the peak flux is a function only of the shape factor f and the half angle θ_s and is not dependent on the diameter of the concentrator. The latter, however, affects the width of the distribution and then the radius of the receiver window. Figure 9 shows the distribution of the solar flux Φ on the focal plane for different values of the diameter D of the parabolic concentrator. The distribution have been calculated in the following conditions: solar radiation 800 W/m^2 , shape factor 0.6, mirror reflectance 0.95, tracking error 7 mrad and, then, r_g/D ratio 0.00705, peak flux 17202 kW/m^2 .

The expressions for the receiver window efficiency and the concentration factor are given by the following relations:

$$\eta_w = 1 - e^{-\frac{r^2}{2\mu^2}} \quad C_w = \frac{\phi^{peak}}{I} \frac{\eta_w}{r^2 / 2\mu^2}$$

In Figure 10, the efficiency of the receiver window and the concentration factor, as a function of the ratio between the radius of the window itself and the standard deviation of the Gaussian distribution, are shown for a concentrator with shape factor equal to 0.6 and in the case: D=5m; r_g=3.525 cm; μ=1.175 cm.

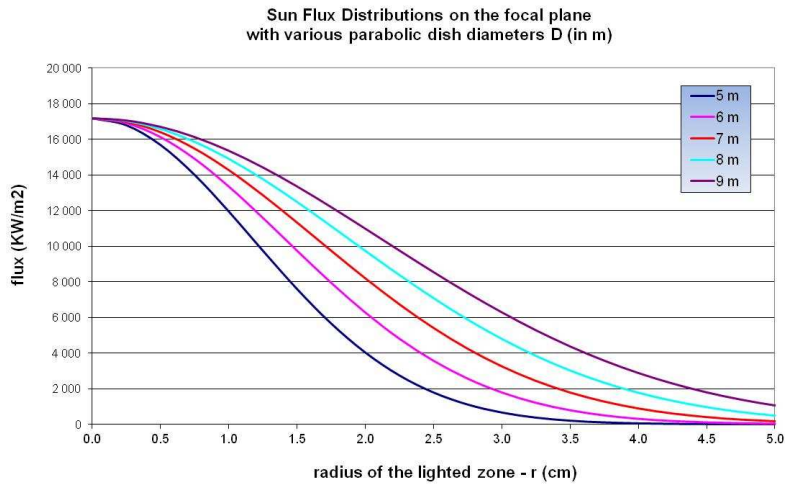


Figure 9 - Gaussian flux distribution on the focal plane

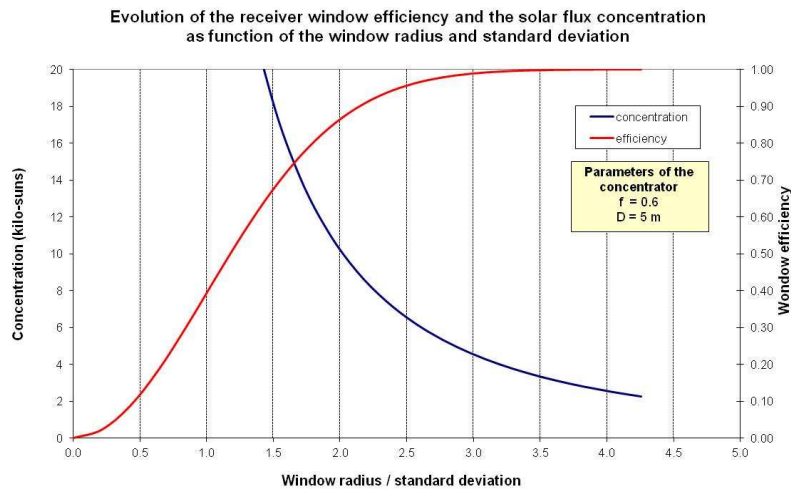


Figure 10 – Receiver window efficiency

As it can be seen, for low values of the ratio r/μ an high concentration factor but low efficiency are obtained while for high values of the ratio (for example, about 3) the efficiency is high but the concentration factor is low. The same type of data (windows efficiency, averaged flux and concentration factor) are shown in Figure 11, Figure 12 and Figure 13 as a function of the receiver window radius and the diameter of the parabolic dish concentrator.

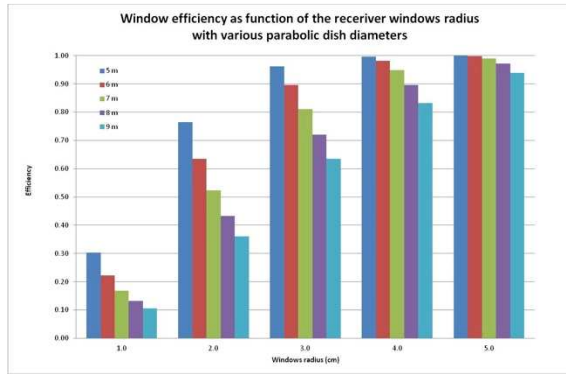


Figure 11 – Receiver window efficiency

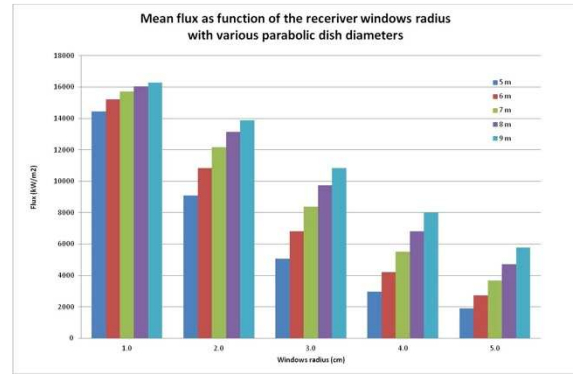


Figure 12 – Averaged flux on the receiver window

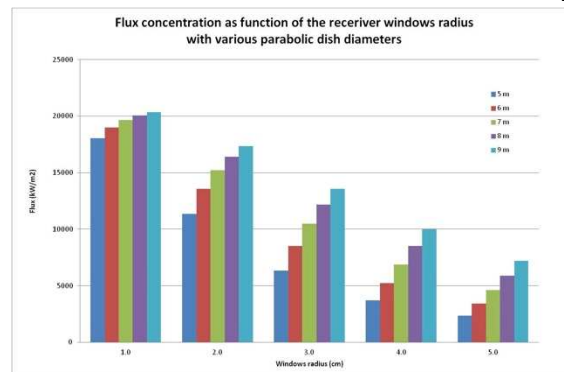


Figure 13 – Concentration factor on the receiver window

Conclusions

The parabolic dish collector performances are strictly dependent on the shape factor and the aperture area diameter. In Table 2 some parabolic dish collector configurations are shown. The evaluations reported in the table have been performed using a 0.6 shape factor, a 800 W/m² solar radiation, a 7 mrad tracking error and a 25% global efficiency. The intercepted sun power has been calculated as: $P_c = (\pi D^2 / 4) I$ where I is the solar radiation.

Dish diameter (m)	Focus distance (m)	r _g (cm)	A aperture (m ²)	Intercepted Sun Power (kW)	Electrical Power (*) (kW)
2	1.20	1.41	3.14	2.51	0.63
3	1.80	2.12	7.07	5.65	1.41
4	2.40	2.82	12.57	10.05	2.51
5	3.00	3.53	19.63	15.71	3.93
6	3.60	4.23	28.27	22.62	5.65
7	4.20	4.94	38.48	30.79	7.70
8	4.80	5.64	50.27	40.21	10.05
9	5.40	6.35	63.62	50.89	12.72
10	6.00	7.05	78.54	62.83	15.71

(*) Calculated in the hypothesis of 25% global efficiency

Table 2 – Parabolic dish collector configuration with shape factor 0.6, 7 mrad tracking error and solar radiation 800 W/m²

As discussed above the best choice to obtain the higher concentration factor is to have a shape factor of about 0.6.

Furthermore, selecting a receiver windows radius equal to the radius r_g, it is possible to maximize the concentration efficiency. Since, once fixed the shape factor (0.6) and the total

tracking error (7mrad), the minimum value for the ratio r_g/D is equal to 0.00705, the selection of the radius r_g is dependent on the diameter: as an example if the selected D is equal to 5 m, the diameter of the receiver window will be about 7 cm, while if D is equal to 8 m, the receiver window diameter will be about 20 cm.

Actually, with the aim of optimizing the overall efficiency of the system, the choice of the receiver window diameter should be made taking into account the energy balance of the receiver and not only the optical aspects. This aspect will be analysed in the following chapter.

Efficiency evaluation

In the following analysis a cavity receiver with an aperture window radius r is considered. The absorption efficiency, defined as the ratio between the useful extracted power and the intercepted solar power is given by:

$$\eta_{ass} = \eta_C * \eta_{in} * \eta_W * \eta_{ca}$$

where:

- η_{ass} : solar energy absorption efficiency
- η_C : concentrator reflection efficiency
- η_{in} : focal plane incident power collection efficiency
- η_W : window transmission efficiency
- η_{ca} : conversion in useful power efficiency

Concentrator reflection efficiency

The ability of the parabolic mirrors to reflect the solar intercepted power P_c to the focal plane (reflectance) is expressed as:

$$\eta_C = \frac{P_{in}}{P_c} = 0.95$$

This efficiency is usually equal to about 95%.

Focal plane incident power collection efficiency

This efficiency is the ratio of the effective power collected by the receiver window P_w and the total power distributed on the focal plane P_{in} . It is a function of the window aperture radius and is equal to:

$$\eta_{in} = \frac{P_w}{P_{in}} = \left(1 - e^{-\frac{r^2}{2\mu^2}} \right)$$

Window transmission efficiency

The window transmission efficiency is the ratio between the power transmitted to the cavity P_{aw} and that incident on the window P_w . Given the complexity of the phenomena of absorption/reflection occurring inside the cavity the transmission efficiency can be assumed equal to the apparent absorbance α_w of the window.

$$\eta_w = \frac{P_{aw}}{P_w} = \alpha_w$$

For a black body, the apparent absorbance is 1.

Conversion in useful power efficiency

The conversion in useful power efficiency is the ratio between the useful power P_u absorbed by the cavity and the power transmitted to the cavity P_{aw} . The useful power is thus a function of the power lost from the cavity. Ignoring losses by conduction and convection, the predominant losses, given the high temperature level, are those due to reirradiation from the cavity through the window aperture P_{rw} :

$$P_{rw} = \sigma \epsilon_w T^4 (\pi r^2)$$

where σ is the Stefan-Boltzman constant and ϵ_w the emissivity of the cavity, that for a black body is 1. So, the cavity efficiency can be expressed in the following way:

$$\eta_{ca} = \frac{P_u}{P_{aw}} = \frac{P_{aw} - P_{rw}}{P_{aw}} = 1 - \frac{P_{rw}}{P_{aw}} = 1 - \frac{\sigma \epsilon_w T^4 (\pi r^2)}{P_{aw}}$$

Absorption efficiency

Taking into consideration the definitions adopted for the different efficiency terms, the complete expression for the absorption efficiency of the concentrator/receiver system is:

$$\eta_{ass} = \eta_C \left(1 - e^{-\frac{r^2}{2\mu^2}} \right) \alpha_w \left(1 - \frac{\sigma \epsilon_w T^4 (\pi r^2)}{P_{aw}} \right)$$

This relation can also be written in the following form:

$$\eta_{ass} = \eta_C \left[\alpha_w \left(1 - e^{-\frac{r^2}{2\mu^2}} \right) - \frac{\sigma \epsilon_w T^4}{2\phi_{in}^{picco}} \left(\frac{r}{\mu} \right)^2 \right]$$

Once the characteristics of the concentrator are fixed, the absorption efficiency is only function of the radius r of the window aperture and the cavity average temperature T .

In Figure 14, the trend of the absorption efficiency as a function of the ratio r/μ for different operating temperatures of the cavity, in the hypothesis that the receiver behaves as a black body, that the concentrator has a shape factor f equal to 0.6 and that the solar irradiation is equal to 800 W/m^2 , is shown.

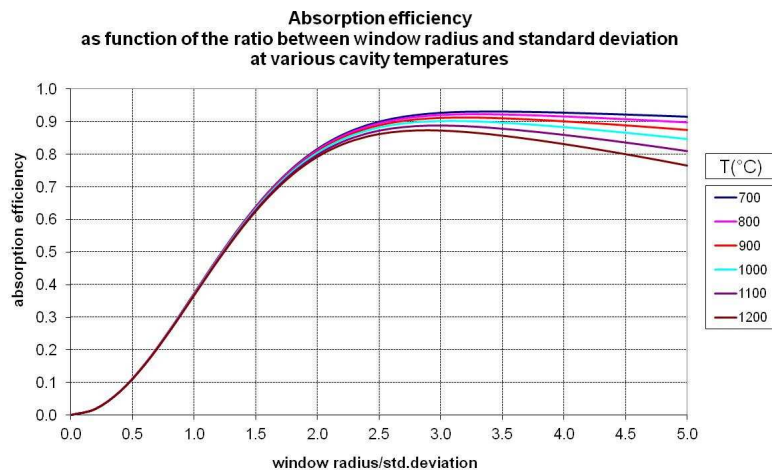


Figure 14 – Absorption efficiency

It can be seen in all reported cases the presence of a maximum for the absorption efficiency. Increasing the cavity temperature, this maximum decreases and shifts to lower values of the r/μ ratio. At temperatures below 1000 °C an efficiency of over 90% is reached at values of r/μ equal to 3, then remaining almost constant.

Maximum cavity temperature

The maximum temperature reached in the cavity is that for which the absorption efficiency is null ($\eta_{\text{ass}} = 0$) or the power absorbed by the cavity equals the power lost by radiation ($P_{\text{aw}} = P_{\text{rw}}$):

$$\alpha_w P_w = \sigma \varepsilon_w T^4 (\pi r^2)$$

from which:

$$T_{\text{max}} = \left(\frac{\alpha_w P_w}{\sigma \varepsilon_w (\pi r^2)} \right)^{1/4} = \left(\frac{\alpha_w \hat{C} I}{\sigma \varepsilon_w} \right)^{1/4}$$

where:

$$\hat{C} = \frac{P_w}{(\pi r^2) I} = \frac{\bar{\phi}_w}{I}$$

represents the concentration factor on the window of the cavity.

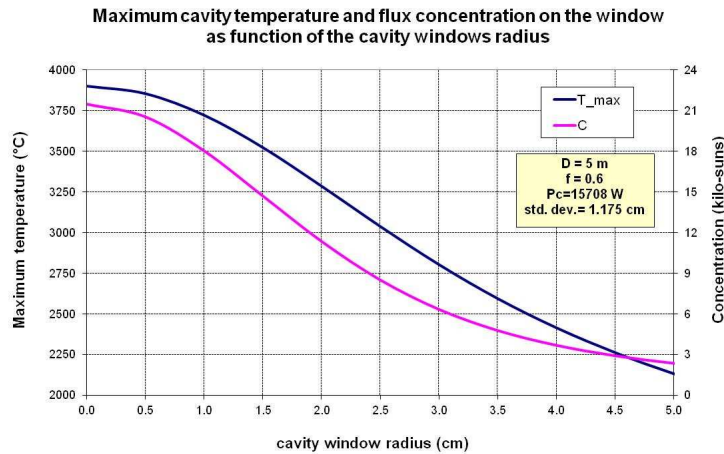


Figure 15 – Maximum cavity temperature and concentration

Total efficiency

The useful power is used as heat in high temperature processes for guiding, for example, endothermic chemical reactions. The conversion of process heat into work or into Gibbs free energy of the reaction products is limited by the efficiency of Carnot. Then, for an ideal system, having indicated with T_L the temperature of the cold sink, the efficiency of Carnot is:

$$\eta_{\text{Carnot}} = 1 - \frac{T_L}{T}$$

Therefore, the total efficiency will be:

$$\eta_{\text{tot}} = \eta_{\text{ass}} \cdot \eta_{\text{Carnot}}$$

In Figure 16, the trend of total efficiency as a function of the ratio r/μ , for different operating temperatures of the cavity, is shown. As it can be seen, the difference between the total efficiency and the absorption efficiency increases as the the temperature of the cavity is reduced. For temperatures between 800 and 1000 °C the total efficiency reaches a maximum of about 65-70%.

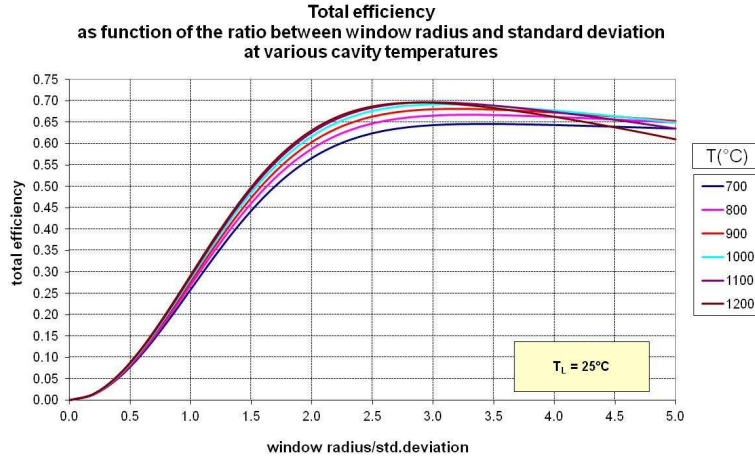


Figure 16 – Total efficiency

Therefore, it is evident, both from the relations previously reported and from the following figures (from Figure 17 to Figure 22), referring to the same conditions as in Figure 14, the total efficiency of the system is highly dependent on the temperature of the cavity and on the radius of the window aperture of the cavity itself. Then, an optimal operative zone exists, where the efficiency reaches its maximum values.

The optimal values for r and T , corresponding to the maximum value of the efficiency, can be found imposing the following conditions:

$$\begin{cases} \frac{\partial \eta_{tot}}{\partial r} = 0 \\ \frac{\partial \eta_{tot}}{\partial T} = 0 \end{cases}$$

From the first condition it is possible to define the optimal value for the window aperture radius:

$$r_{opt} = \left[-2\mu^2 \ln(X(T_{opt})) \right]^{0.5}$$

where :

$$X(T) = \frac{\epsilon_w \sigma T^4}{\alpha_w \phi_{in}^{picco}}$$

while, from the second condition, a not explicit relation allows, using an iterative procedure, to find the optimal value for the temperature:

$$(4T - 3T_L)X(T) \ln(X(T)) + T_L(1 - X(T)) = 0$$

A possible iterative schema is the following:

$$\begin{aligned} T^{(0)} &= T_{max} / 2 \\ T_0^{(i)} &= \frac{T_L}{4} \left[3 - \frac{(1 - X(T^{(i-1)}))}{X(T^{(i-1)}) \ln(X(T^{(i-1)}))} \right] \\ \Delta T^{(i)} &= T_0^{(i)} - T^{(i-1)} \\ T^{(i)} &= T^{(i-1)} + 0.3 \Delta T^{(i)} \\ \text{for } i &= 1, \dots, n \end{aligned}$$

As an example, in the case shown in the following figures, the optimum operative temperature of the cavity is 1167 °C and the optimum window radius is 3.5 cm.

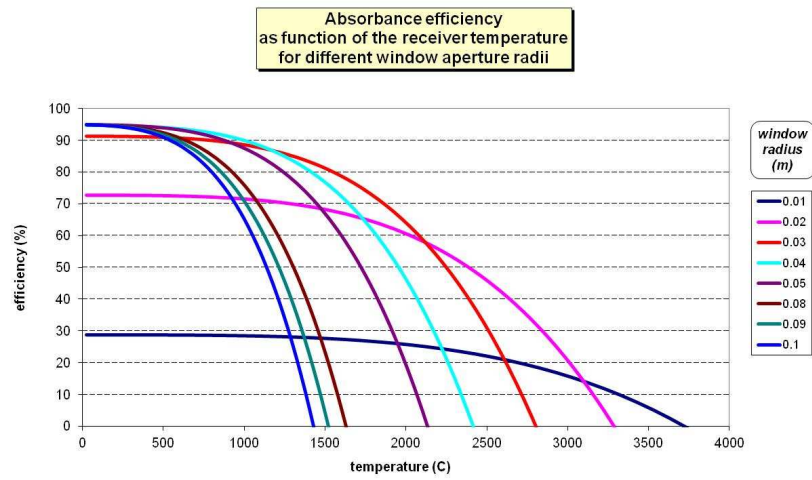


Figure 17

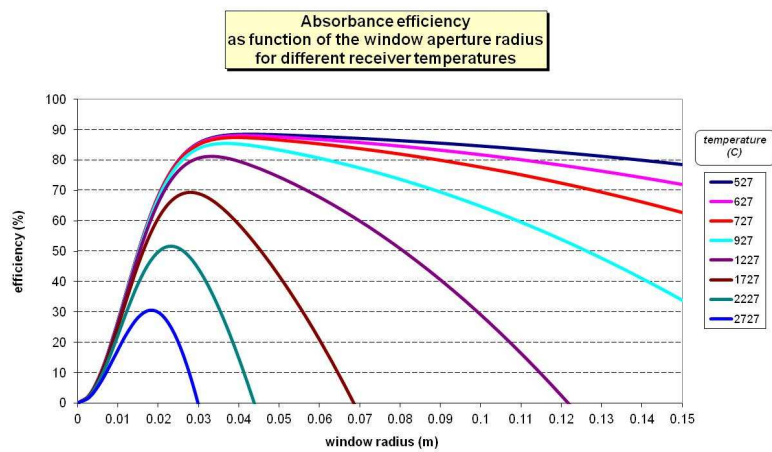


Figure 18

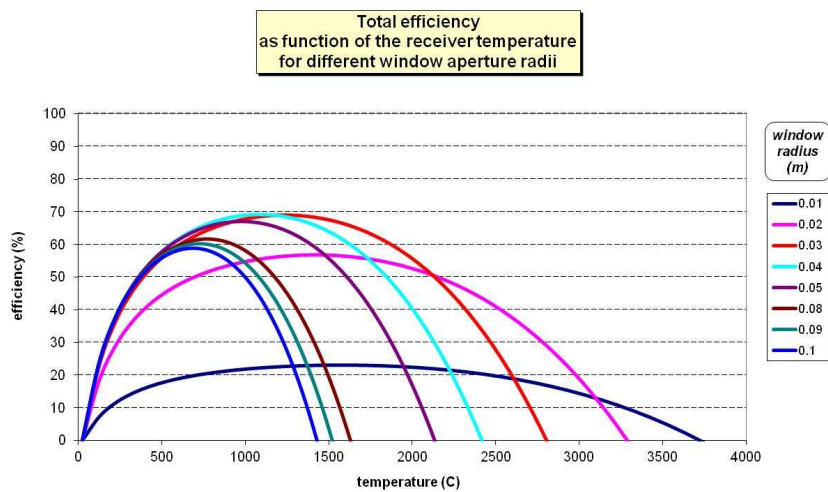


Figure 19

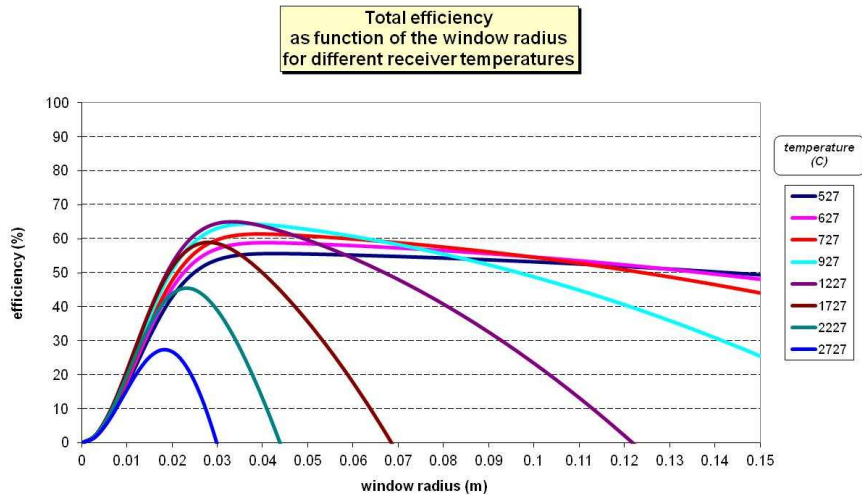


Figure 20

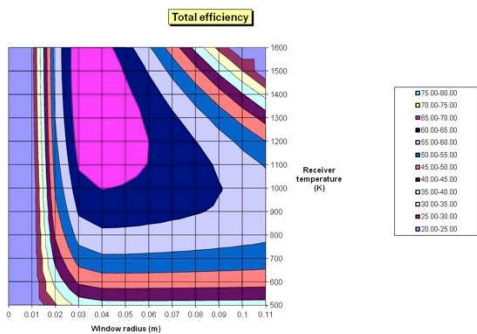


Figure 21

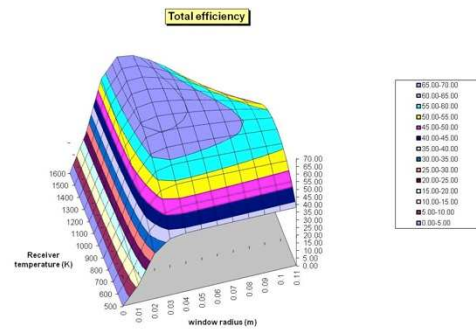


Figure 22

Application of the “ray tracing” method

The purpose of this section is to assess the optical performance of a dish concentration system, using the method of ray tracing, in order to:

- check the reliability of the results obtained through the simplified models previously developed and applied;
- compare the optical behavior of dish systems with different shapes (parabolic surface vs spherical surface), in order to introduce technological simplifications to obtain a reduction of manufacturing costs.

The application of this method has been achieved through the use of a software tool named **SolTrace** developed at the National Renewable Energy Laboratory (NREL).

SolTrace has been developed to model concentrating solar power (CSP) systems and analyze their optical performance.

Although ideally suited for solar applications, the code can also be used to model and characterize many general optical systems. The creation of the code evolved out of a need to model more complex solar optical systems than those that could be modeled with existing tools.

The code uses Monte Carlo ray-tracing methodology. The user selects a given number of rays to be traced. Each ray is traced through the system while encountering various optical interactions.

General settings

The optical behavior of a dish concentrator, characterized by the following main parameters, has been simulated:

Parameter	Value
Aperture diameter (m)	5
Aperture area (m ²)	19.635
Focal plane quote (m)	3
Direct Normal Irradiance - DNI (W/m ²)	1000
Intercepted solar power (W)	19635
Number of traced solar rays	1000000
Power for each solar ray	0.019635
Mirror reflectivity	0.95
Sun shape error (mrad)	2.73
Mirror slope error (mrad)	3.22
Mirror specularity (mrad)	0
Mirror optical error (mrad)	6.44
Total tracking error (mrad)	7

Table 3 – Main parameters used in the SolTrace simulations

As stated in the simplified models, the total tracking error is 7 mrad.

To obtain this error the sun shape and optical errors (mirrors, slope and specularity) have been assigned to satisfy the following relationship:

$$\sigma_{tot} = \sqrt{\sigma_{sun}^2 + \sigma_{opt}^2} = \sqrt{\sigma_{sun}^2 + 4\sigma_{slope}^2 + \sigma_{spec}^2} \quad (mrad)$$

Parabolic shape dish concentrator: simplified model versus ray-tracing model

The optical behavior of a parabolic dish concentrator, using different receiver window diameters, has been simulated. The main results are shown in Table 4 and plotted in Figure 23. Instead, in Figure 24 and Figure 25 the interception points, on the dish and the focal plane, along with the focal flux distribution are shown for 7 cm and 10 cm receiver window diameter respectively. Based on the results it is possible to make the following considerations:

- The interception factor increases, from 54% to 88%, when the receiver window diameter increases. Of course, the optical efficiency shows the same trend (from 51% to 83%).
- On the contrary, the concentration factor decreases (from 3700 to 2200 suns) when the receiver window diameter increases.
- Larger is the receiver window diameter higher is the optical efficiency and lower the concentration (and hence the maximum reached temperatures). Moreover, when the receiver window diameter increases, energy losses increases and the total efficiency of the system lowers.
- Considering a receiver window diameter of 7 cm (optimized value for a dish diameter of 5 m, calculated through the simplified method described in the previous paragraphs), an optical efficiency of 61% and a concentration factor of 3300 has been obtained.

Receiver window diameter	Receiver window area	Geometrical concentration	nr. of rays on the focal plane	power on the focal plane	Interception factor	Average flux	Optical efficiency	Concentration
<i>m</i>	<i>m²</i>	<i>suns</i>	-	<i>W</i>	-	<i>W/m²</i>	-	<i>suns</i>
0.06	0.002827	6944	535767	10519	0.536	3.72E+06	0.509	3721
0.07	0.003848	5102	646364	12691	0.646	3.30E+06	0.614	3298
0.08	0.005027	3906	741288	14555	0.741	2.90E+06	0.704	2896
0.09	0.006362	3086	817660	16054	0.818	2.52E+06	0.777	2524
0.1	0.007854	2500	876376	17207	0.876	2.19E+06	0.833	2191

Table 4 – Results of the optical simulation of the parabolic dish collector

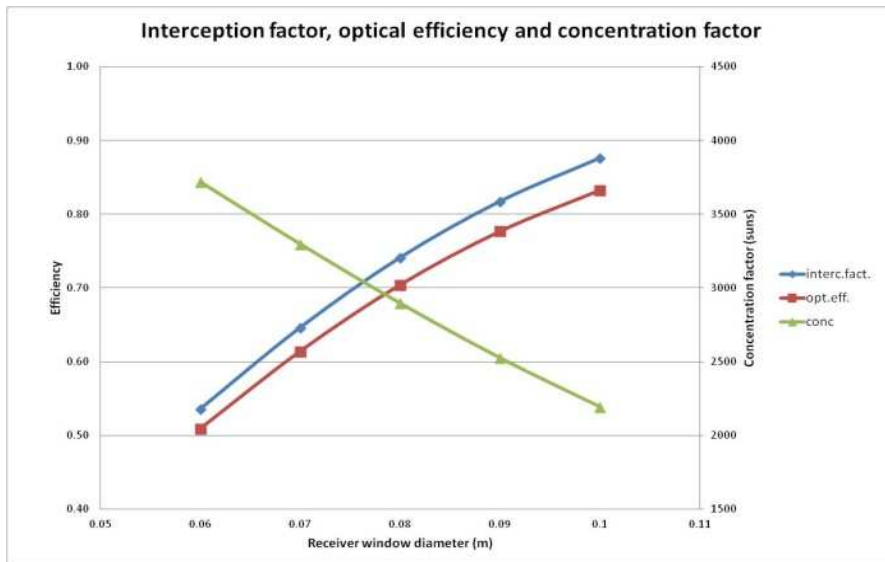


Figure 23

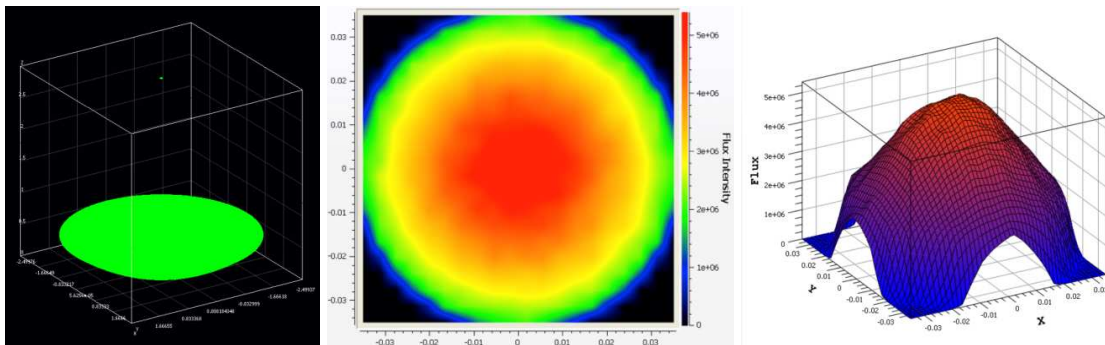


Figure 24 – Parabolic dish interception points and flux distribution for a 7 cm receiver window diameter

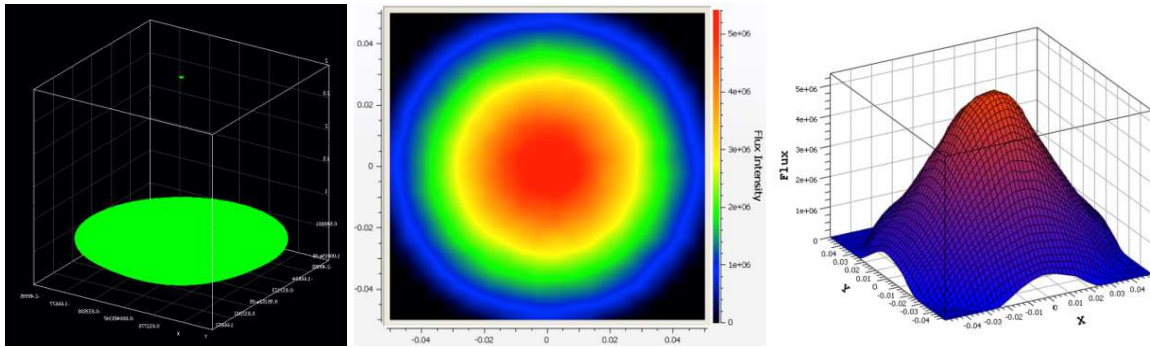


Figure 25 - Parabolic dish interception points and flux distribution for a 10 cm receiver window diameter

The concentration factor calculated through the ray tracing method is very close to that determined using the simplified method. Instead, the optical efficiency calculated through the simplified model is higher than the one obtained through the ray-tracing method (Figure 26). This is substantially due to the fact that the source (the sun) and the reflection are considered statistically influenced by a Gaussian distribution which tends to give a lower aberration of the sun image. This result has been taken into account for the improvement of the simplified model, as presented in the paragraph "Performance analysis".

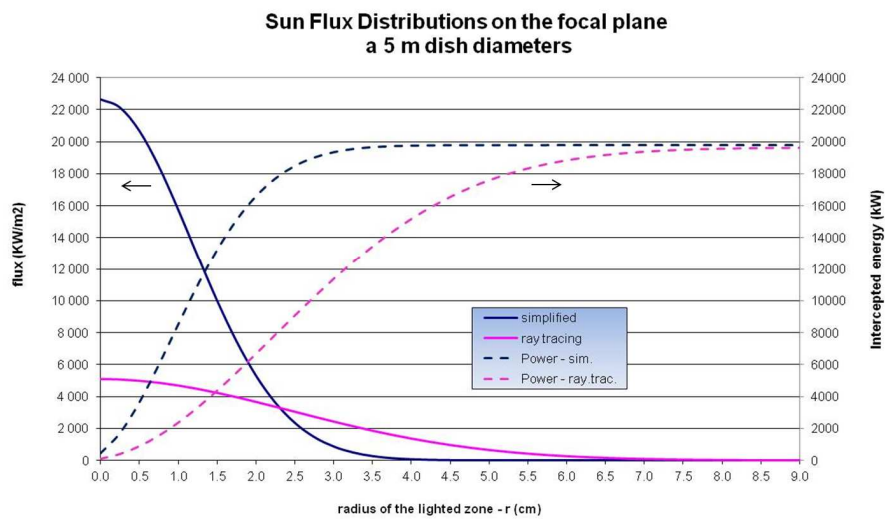


Figure 26 – Results comparison for simplified and ray tracing methods

Spherical shape dish concentrator

The ideal shape of a parabolic dish concentrator is surely a paraboloid of revolution. The surface so generated has the characteristic to have a variable curvature from the center of the disc to its periphery. This could represent a problem especially in the production of large reflective surfaces.

The possibility to approximate such a parabolic surface with a spherical one, at constant curvature, would represent a simplification in terms of construction technology with a consequent lowering of the production costs.

The main drawback, being no longer a figure with a punctual fire, might be to have an aberration of the sunlight beams with a significant loss of efficiency.

Then, with the aim of evaluating the different performance of the parabolic and spherical concentrators, some optical simulations, described below, have been conducted. In this analysis, for the same aperture area, the paraboloid of revolution is replaced by a spherical surface having a radius two times the focal distance ($r = 2f$).

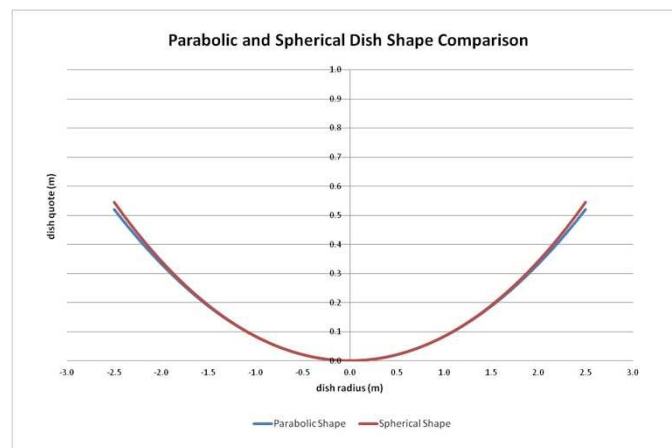


Figure 27

In Figure 27 both surfaces are compared. From the figure it is evident the substantial overlap in the central part of the dish. On the contrary the peripheral section of the spherical surface turns out to be more closed with respect to the paraboloid. This will have the effect of producing an intersection of the light beams at lower altitudes to the focal plane and thus a greater enlargement of the focal spot, i.e. higher losses.

To quantify this effect a series of simulations, in perfect analogy with the preceding part, has been performed, where the diameter of the receiver window (7 cm) is maintained constant and the effect of a possible lowering of the focal plane has been analyzed.

In Table 5, Figure 28, Figure 29 and Figure 30 all the main results are shown.

We clearly note how the interception factor, the optical efficiency and the concentration ratio are lower (about half) compared to the parabolic dish calculations (focal plane at 3 m high, see Table 4). Their maximum values are: from 0.21 to 0.38 for the interception factor, from 20% to 36% for the optical efficiency and from 1060 to 1915 suns for the concentration ratio (in the case of parabolic surface the concentration factor is equal to 3298).

The maximum value for these quantities is obtained with a focal plane positioned at a lower level and equal to about 2.88 cm, this resulting in the optimal point (see Figure 28).

Thus, it is evident that the possible technological simplification involves a significant loss in terms of efficiency of the system and therefore of available useful energy.

Receiver window quote	Receiver window area	Geometrical concentration	nr. of rays on the focal plane	power on the focal plane	Interception factor	Average flux	Optical efficiency	Concentration Ratio
<i>m</i>	<i>m2</i>	<i>suns</i>	-	<i>W</i>	-	<i>W/m2</i>	-	<i>suns</i>
3	0.003848	5102	207486	4073	0.207	1.06E+06	0.197	1059
2.95	0.003848	5102	297965	5850	0.298	1.52E+06	0.283	1520
2.9	0.003848	5102	367476	7215	0.367	1.87E+06	0.349	1875
2.88	0.003848	5102	375227	7367	0.375	1.91E+06	0.356	1914
2.85	0.003848	5102	361029	7088	0.361	1.84E+06	0.343	1842
2.8	0.003848	5102	285113	5598	0.285	1.45E+06	0.271	1455

Table 5 – Results of the optical simulation of the spherical dish collector

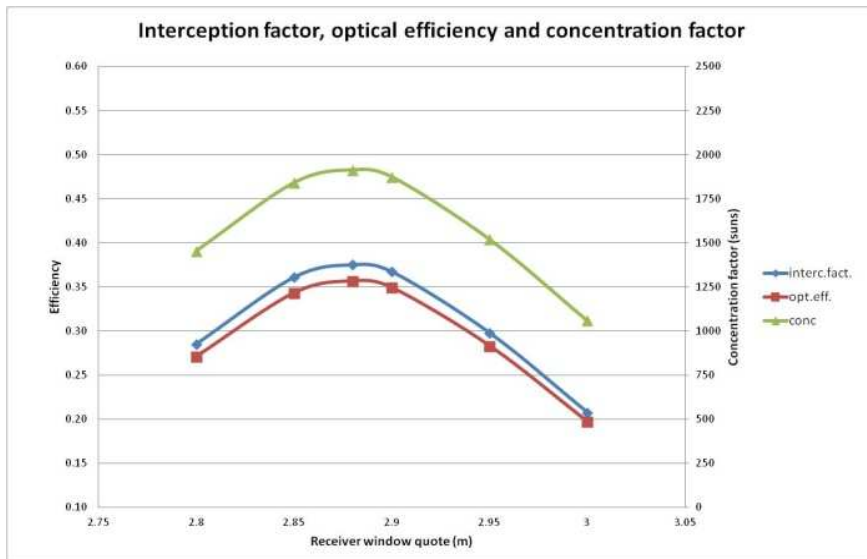


Figure 28: Results of the optical simulation of the spherical dish collector

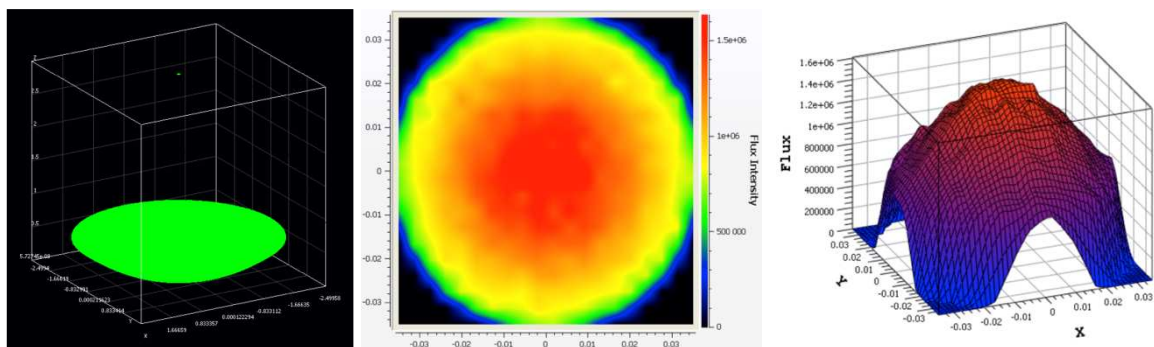


Figure 29 - Spherical dish interception points and flux distribution for a 3 m focus plane quote

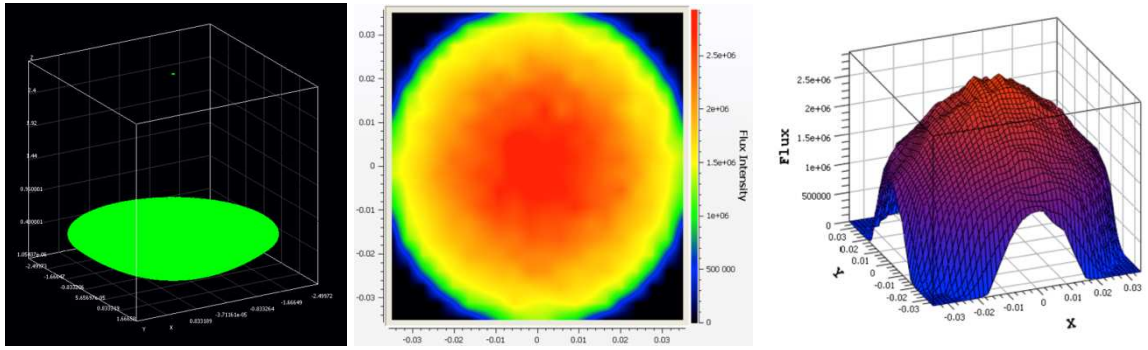


Figure 30 - Spherical dish interception points and flux distribution for a 2.88 m focus plane quote

Conclusions

In this chapter, a simplified optical model able to optimize the optical performance of a parabolic dish concentrator through the determination of the optimum shape of the concentrator and the optimum diameter of the receiver window has been developed.

Furthermore optics numerical simulations, based on the use of the SolTrace tool (ray tracing method), have been carried out in order to evaluate both the reliability of the simplified formulation and the possibility to approximate the parabolic surface with a spherical one. The performed analyses show that the simplified formulation, compared with the "ray tracing" simulations, tends to overestimate the optical efficiency of the system by a factor close to 2. Assuming that the ray tracing model results are more reliable, it is desirable to use the numerical prediction to determine the solar flux distribution, and then the theoretical evaluation of the window efficiency, to predict the performance of the collector as a whole. Alternatively, the starting hypothesis assumed for the development of the simplified model, that is $r_g = 3\mu$, should be reviewed with a less "optimistic" hypothesis in which the following equivalence could be assumed: $2r_g = 3\mu$. In this case there would be a good correspondence between the simplified method and ray tracing method results (Figure 31).

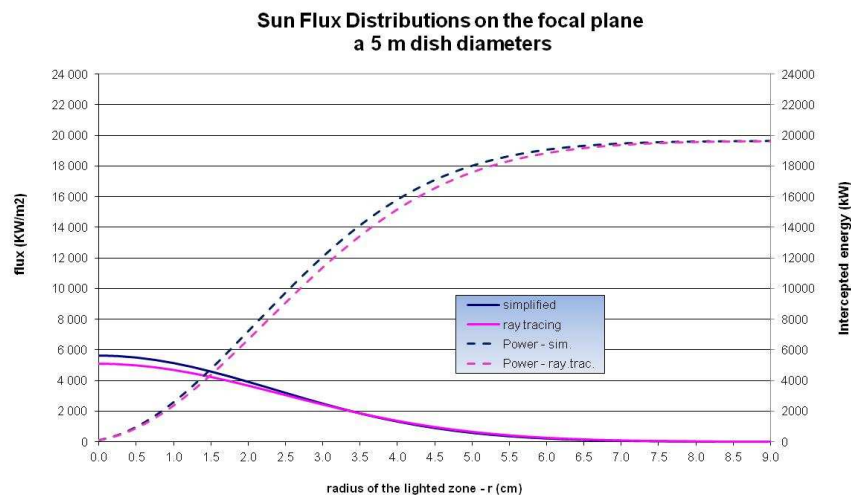


Figure 31 - Results comparison for simplified and ray tracing method with the new hypothesis

However, thanks to this starting approach to the optimization of a parabolic dish collector, despite the showed differences, some considerations of general validity can be made:

- The optimal shape of the parabola, in order to have high concentration ratio and high temperatures, must have a focus/diameter ratio close to 0.6;
- A parabolic surface of revolution is approximated by a spherical surface only if a strong reduction in efficiency of the system, caused by a very high aberration, can be accepted.

Clearly, all the evaluations linked to the optimal size of the receiver window and its optical efficiency should be revised once the experimental distribution of the solar flux is available.

Performance analysis

In the present paragraph a performance analysis of the solar dish collector proposed by Innova will be reported.

As a starting hypothesis it has been assumed to use a 7kWe MGT with the following base conditions: maximum solar radiation (I) of about 800 W/m^2 , maximum global efficiency (η_{tot}) of about 20%, and utilization factor of the total area (f_{used}) of 90%.

In this case, we should get:

- A useful receiving surface: $S_{\text{net}} = P_e / (\eta_{\text{tot}} I) = 43.75 \text{ m}^2$;
- A total receiving surface: $S_{\text{tot}} = S_{\text{net}} / f_{\text{used}} = 48.6 \text{ m}^2$;
- An aperture diameter of the parabolic dish: $D = (4 * S_{\text{tot}} / \pi)^{0.5} = 7.9 \text{ m}$

On the base of this initial rough evaluation, the PDC diameter has been estimated greater than 8 m.

Innova has proposed to develop a 12 m nominal diameter PDC, derived from a system realized by Tessera Solar (Figure 32). This system is able to provide the maximum power required by our application assuring a good margin of flexibility, as reported in the following analysis.



Figure 32- SunCatcher System (Tessera Solar)

Scope of the present paragraph, indeed, is to evaluate the optical and thermal performances of the Innova 12m PDC that will be installed at the Enea Casaccia site.

Dimensions of the Innova PDC

Innova PDC is intended to be composed of two circular crowns of mirrors (Figure 33) that concentrate the sun rays on a power central unit (PCU) located on the focus of the paraboloid. The focus/diameter ratio should be about 0.6, which has been demonstrated to be the optimal shape of the parabola to achieve the highest concentration ratio and the highest temperatures (see the previous paragraphs).

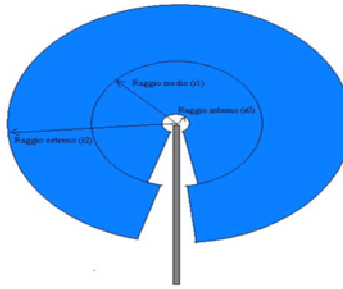


Figure 33 – Schematic of the proposed Innova PDC

The main geometrical characteristics are:

Geometrical characteristic	Value
External diameter (m)	11.73
Mean diameter (m)	6.96
Internal Diameter (m)	2.12
Focus quote (m)	7.04
Shape ratio (F/D)	0.6
Collector rotation center (H) (m)	5.75
Effective aperture area (m ²)	96.14
Nominal aperture area (m ²)	108.1
Aperture area reduction	0.89

Table 6 – Innova Parabolic Dish Collector characteristics

Focal plane flux distribution using a ray-tracing method

The optical performance and the flux distribution on the focal plane have been estimated through the use of an optical model based on the ray tracing method. In particular a software tool named SolTrace, described in the previous paragraphs, has been adopted. Since one of the parameters that most affect the flux distribution is the tracking error, two different analysis with errors of about 7 and 10 mrad respectively have been performed.

To obtain this error values the sun shape and optical errors (mirrors slope and specularity) have been assigned to satisfy the following relationship:

$$\sigma_{tot} = \sqrt{\sigma_{sun}^2 + \sigma_{opt}^2} = \sqrt{\sigma_{sun}^2 + 4\sigma_{slope}^2 + \sigma_{spec}^2} \quad (mrad)$$

The main parameters used in the calculation are listed in the table below.

Parameter	Value
Aperture diameter (m)	11.73
Aperture area (m ²)	108.06
Focal plane quote (m)	7.04
Direct Normal Irradiance - DNI (W/m ²)	1000
Intercepted solar power (W)	108065
Number of traced solar rays	1000000
Power for each solar ray	0.10806

Mirror reflectivity	0.95
Sun shape error (mrad)	2.73
Mirror slope error (mrad)	3.4 (4.6)
Mirror specularity (mrad)	1.2 (3.3)
Mirror optical error (mrad)	6.9 (9.8)
Total tracking error (mrad)	7.43 (10.14)

Table 7 – Main parameters used in the SolTrace simulations

PDC with a 7 mrad total tracking error

The main Soltrace results obtained in the case of a total tracking error of 7 mrad are shown in Figure 34: the interception points, on the dish and on the focal plane, and the focal flux distribution on the focal plane.

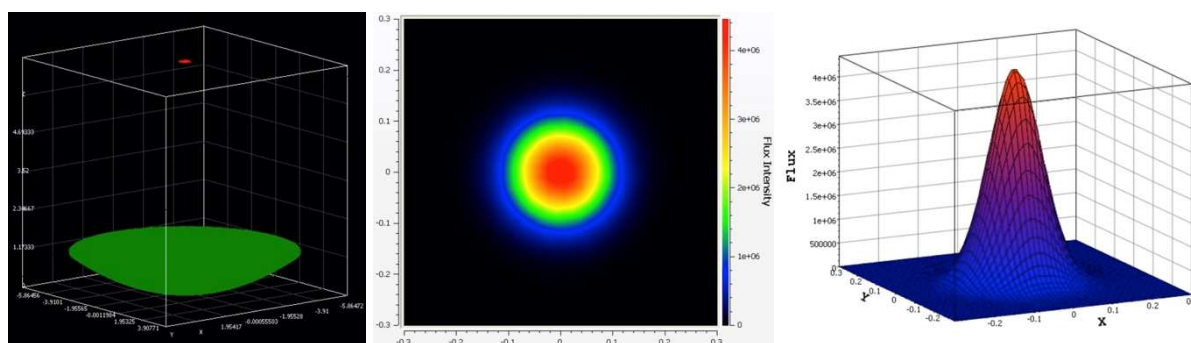


Figure 34 – Parabolic dish interception points and flux distribution in the case of a 7mrad total tracking error

Taking into account the flux distribution generated by Soltrace (red dots in Figure 35), it is possible to evaluate the Gauss distribution parameters that approximate (blu line in Figure 35) the calculated curve. In this case the Gauss parameters are:

$$\phi^{peak} = 4450 \text{ kW/m}^2$$

$$\mu = 0.06044 \text{ m}$$

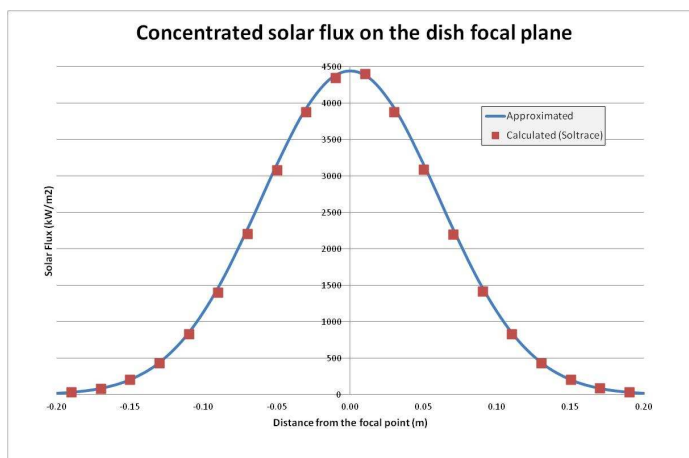


Figure 35 – Calculated (with Soltrace) and approximated Gauss flux distributions(7mrad)

The ratio between the peak flux (Φ^{peak}) and solar radiation (I) provides the maximum achievable concentration value that, in this case, is about 4450 suns.

PDC with a 10 mrad total tracking error

The main Soltrace results obtained in the case of a total tracking error of 10 mrad are shown in Figure 36: the interception points, on the dish and on the focal plane, and the focal flux distribution on the focal plane.

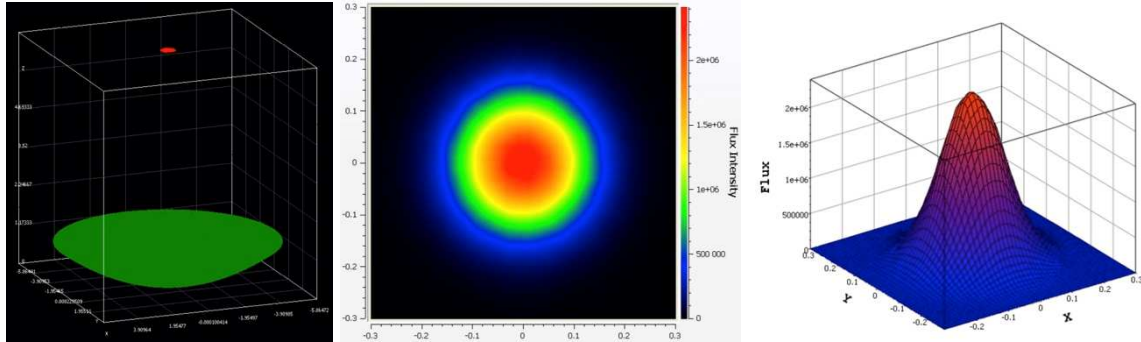


Figure 36 – Parabolic dish interception points and flux distribution in the case of a 7mrad total tracking error

Taking into account the flux distribution generated by Soltrace (red dots in Figure 37), it is possible to evaluate the Gauss distribution parameters that approximate (blu line in Figure 37) the calculated curve. In this case the Gauss parameters are:

$$\begin{aligned}\phi^{peak} &= 2390 \text{ kW/m}^2 \\ \mu &= 0.08241 \text{ m}\end{aligned}$$

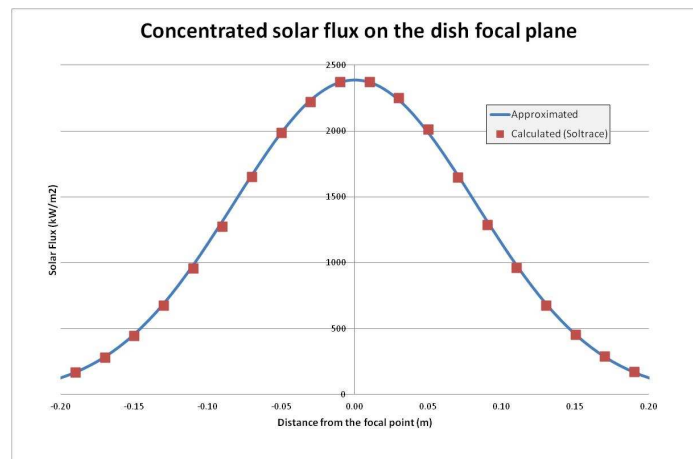


Figure 37 – Calculated (with Soltrace) and approximated Gauss flux distributions(7mrad)

The ratio between the peak flux (Φ^{peak}) and solar radiation (I) provides the maximum achievable concentration value that, in this case, is about 2390 suns.

Efficiency evaluation

In the previous paragraphs the parameters of the Gaussian distribution that represents the distribution of the concentrated solar flux at the focal plane for the Innova dish have been evaluated.

This was done for two different values of tracking errors: 7 and 10 mrad.

In the following table the results obtained are listed:

Total tracking error (mrad)	7	10
Peak flux (kW/m ²)	4450	2390
Standard deviation μ (m)	0.06044	0.08241

Table 8 – Gauss distribution parameters for Innova 12m PDC

The next step, necessary to evaluate the optical and thermal performance of the PDC system, is to estimate its efficiency when a cavity receiver with an aperture window having radius r is placed on the focus of the parabola.

Considering the definition of reflection, collection, window transmission and conversion efficiencies provided in the previous paragraphs, it is possible to calculate the overall absorption efficiency as a function of the windows radius r for different operating temperatures of the cavity, in the hypothesis that the receiver behaves as a black body, that the concentrator has a shape factor f equal to 0.6 and that the solar flux is equal to 800 W/m². The results of the analysis is represented in Figure 38 and Figure 39 for a total tracking error of 7 mrad and 10 mrad respectively. In the figures the presence of a maximum can be seen for all the reported cases. It is evident that this maximum decreases and shifts to lower values of r with the increase of the cavity temperature.

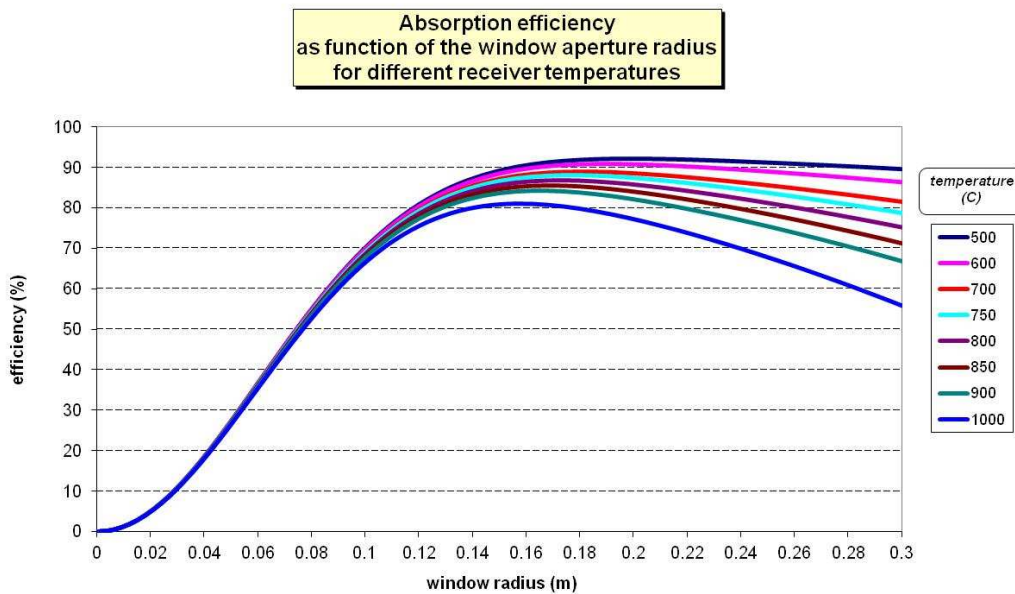


Figure 38 – Absorption efficiency for 7 mrad total tracking error

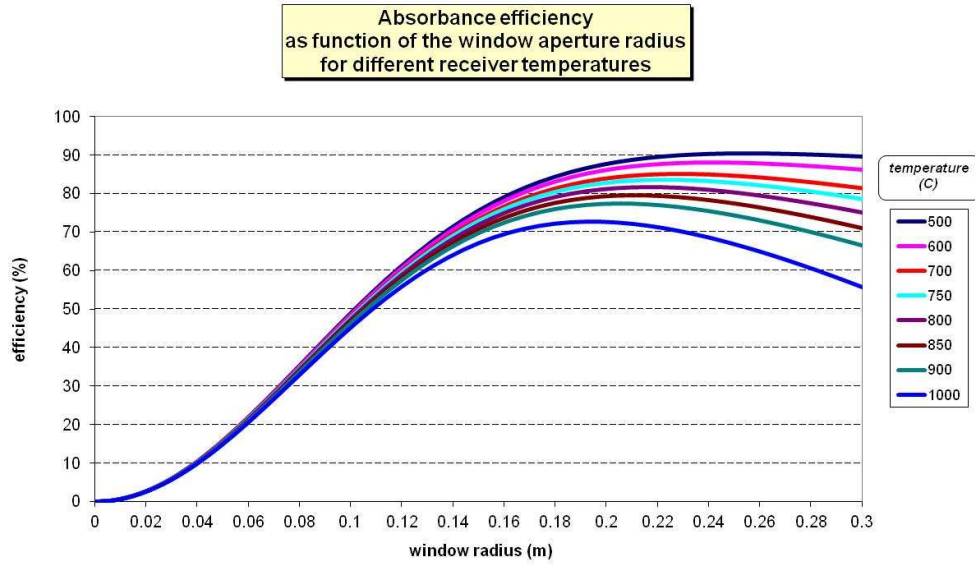


Figure 39 – Absorption efficiency for 10 mrad total tracking error

Maximum cavity temperature

As mentioned in the previous paragraphs, the maximum temperature reached in the cavity is the one for which the absorption efficiency is null ($\eta_{\text{ass}} = 0$) or the power absorbed by the cavity equals that lost by radiation ($P_{\text{aw}} = P_{\text{rw}}$):

$$\alpha_w P_w = \sigma \epsilon_w T^4 (\pi r^2)$$

from which:

$$T_{\text{max}} = \left(\frac{\alpha_w P_w}{\sigma \epsilon_w (\pi r^2)} \right)^{1/4} = \left(\frac{\alpha_w \hat{C} I}{\sigma \epsilon_w} \right)^{1/4}$$

where

$$\hat{C} = \frac{P_w}{(\pi r^2) I} = \frac{\bar{\phi}_w}{I}$$

represents the concentration factor on the window of the cavity. The results of the analysis are reported in the following figures.

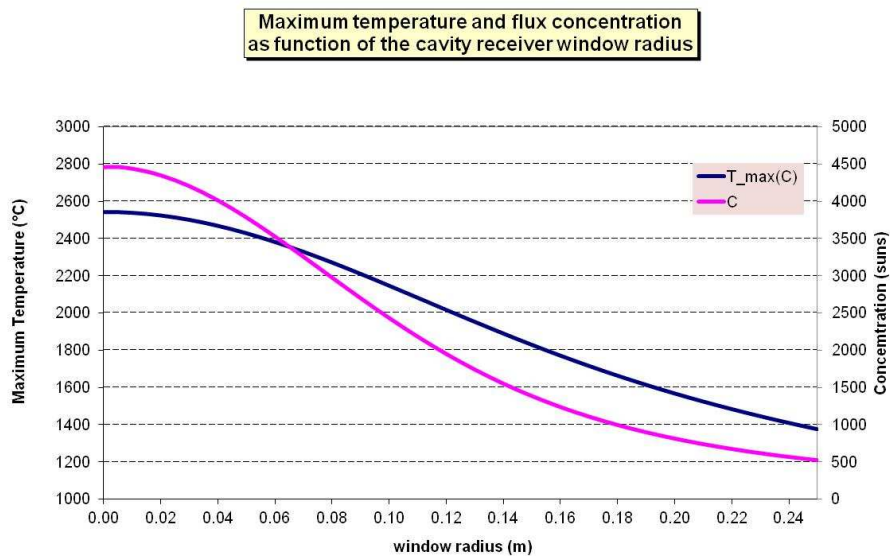


Figure 40 – Maximum cavity temperature and concentration (7 mrad)

Maximum temperature and flux concentration as function of the cavity receiver window radius

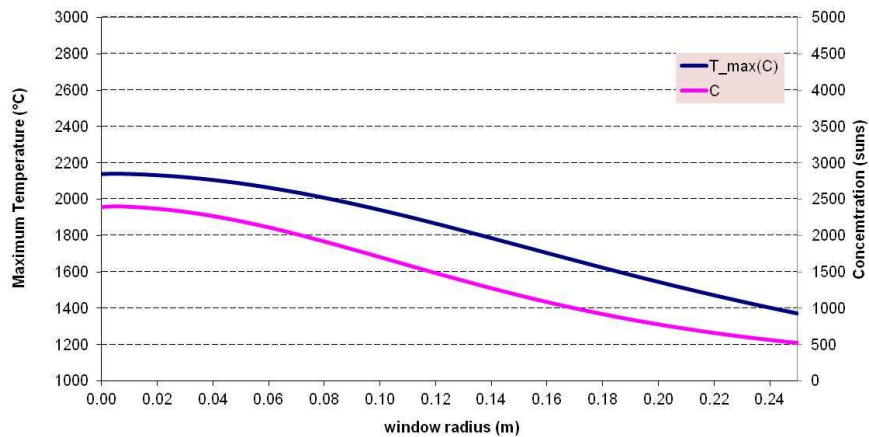


Figure 41 – Maximum cavity temperature and concentration (10mrad)

Total efficiency

As already mentioned in the previous paragraph, the total efficiency, defined as the ratio between the work produced by the process and the solar intercepted power, can be calculated through the following expression:

$$\eta_{tot} = \eta_{ass} \cdot \eta_{Carnot}$$

In Figure 42 and Figure 43, the trend of the total efficiency as a function of the window radius r , for different operating temperatures of the cavity, is shown.

As it can be seen, the difference between the total efficiency and the absorption efficiency increases as the the temperature of the cavity is reduced.

Therefore, it is evident, from the following figures, that the total efficiency of the system is highly dependent on the temperature of the cavity and on the radius of the window aperture of the cavity itself. Then, an optimal operative zone exists, where the efficiency reaches its maximum values.

As already mentioned in the paragraph “Dish shape optimization”, the optimal values for r and T , corresponding to the maximum value of the efficiency, can be found imposing the following conditions:

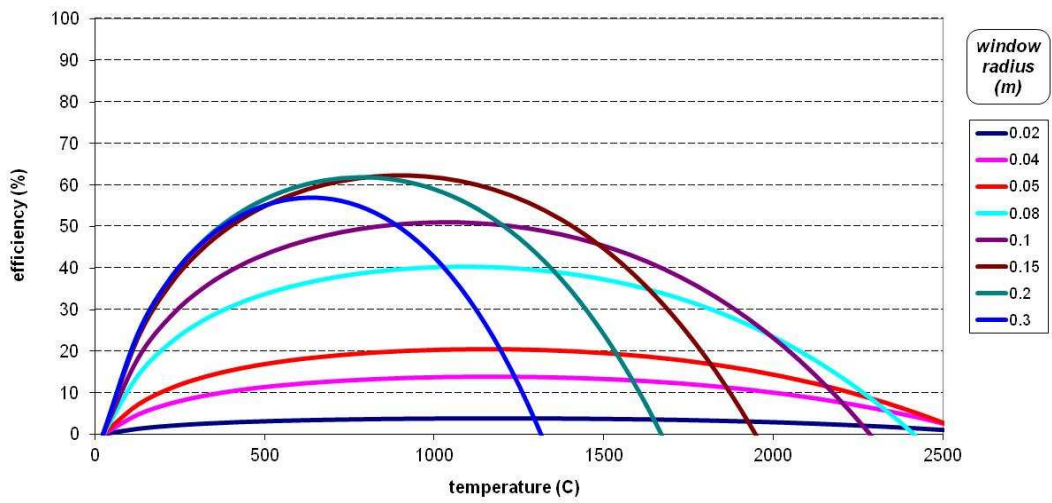
$$\begin{cases} \frac{\partial \eta_{tot}}{\partial r} = 0 \\ \frac{\partial \eta_{tot}}{\partial T} = 0 \end{cases}$$

As an example, in the following table, the optimum operative temperature and receiver window diameter, calculated through the solution of the two equations above mentioned, are reported for a total tracking error of 7 and 10 mrad.

Total tracking error (mrad)	7	10
Cavity temperature (°C)	857	740
Windows diameter (m)	0.34	0.44
Total efficiency (%)	63	59

Table 9 – Optimum operative conditions for Innova 12m PDC

Total efficiency
as function of the receiver temperature
for different window aperture radii



Total efficiency
as function of the window radius
for different receiver temperatures

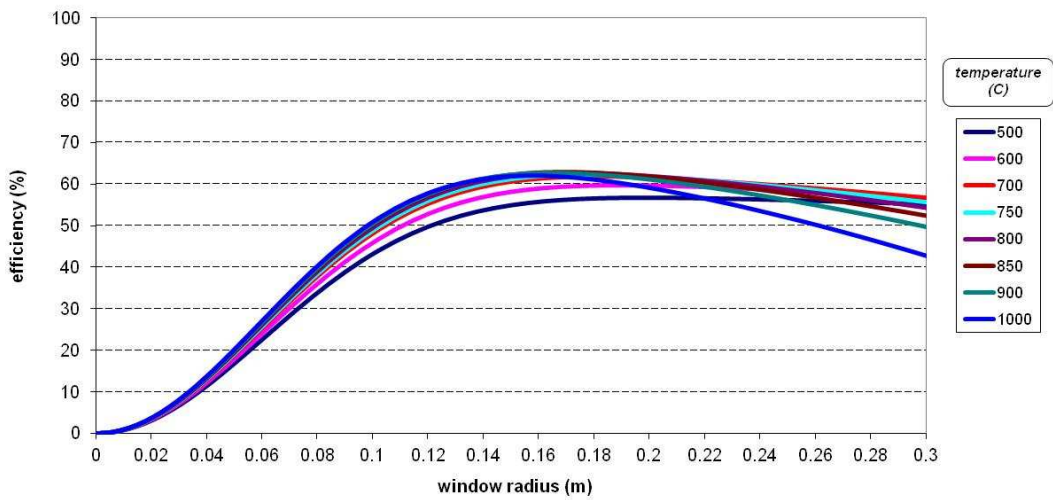


Figure 42 – Total efficiency for 7 mrad total tracking error

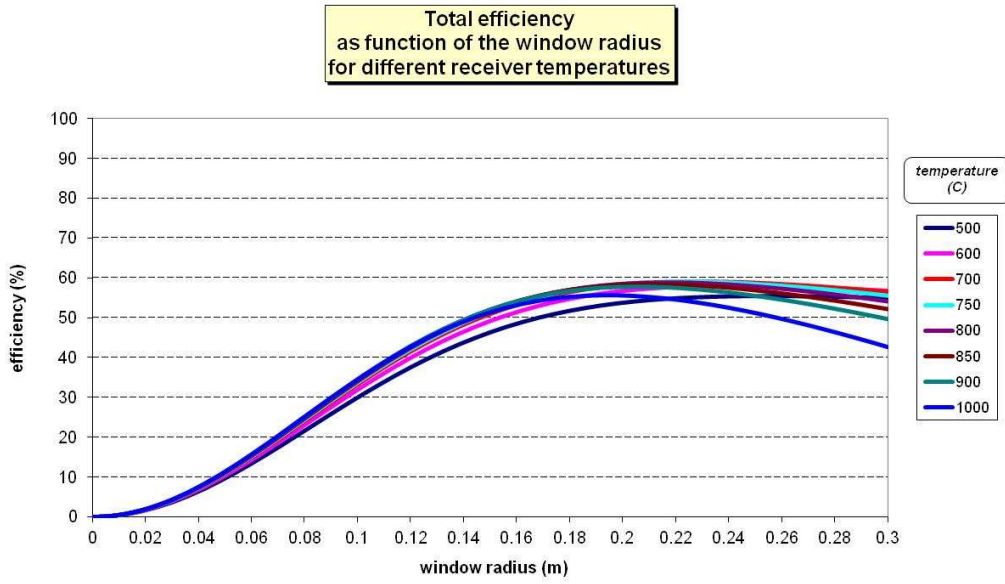
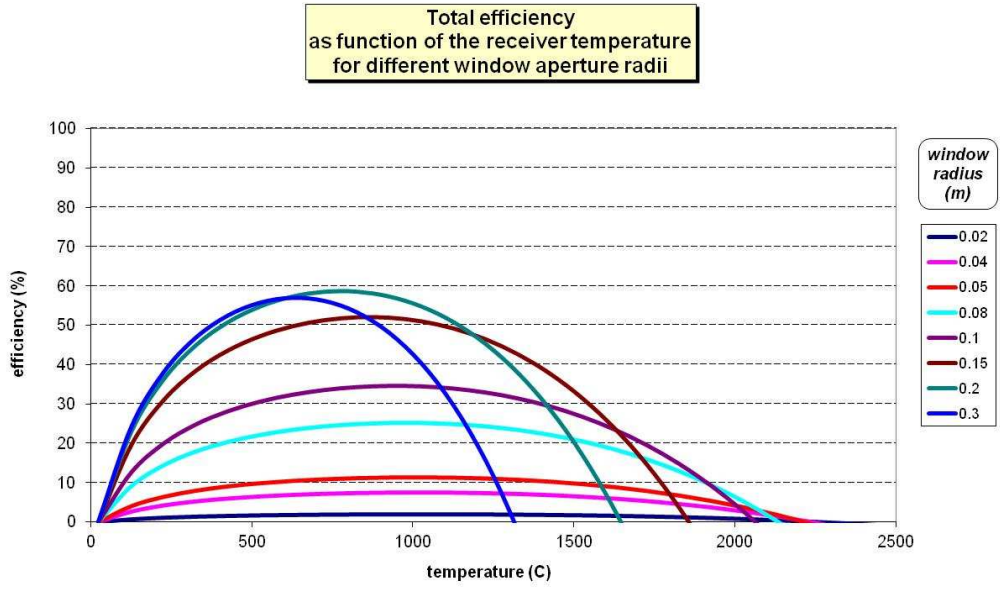


Figure 43 – Total efficiency for 10 mrad total tracking error

Conclusions

In this paragraph, the optical and thermal performances of the dish concentrator proposed by Innova, that will be installed at the Enea Casaccia site, has been analyzed in the hypothesis to have a 7 or 10 mrad total tracking error.

If a window of **20 cm diameter** ($r = 0.1 \text{ m}$) is assumed for the receiver, the calculated performance of the whole system (dish and receiver) can be summarized in Table 10.

To comment on these results, it is worth noticing that, in order to properly run the microturbine-receiver system, the input power available at the receiver window should be about 57 kW, with a concentration factor greater than 1200 suns, for reaching an input power at the microturbine of approximately 40 kW.

In both analyzed cases the concentration factor turns out to be higher than 1200 suns (2168 and 1515 suns respectively). Differently, the power at the receiver window entrance is close to that requested (54.5 kW) only in the case of tracking error equal to 7 mrad. When this error is about 10 mrad the collection efficiency is too small to allow the interception of a power exceeding 40 kW.

Regarding, instead, the thermal power available for the microturbine, this is surely higher than requested in the case of the 7 mrad (52 kW) and slightly lower in the case of 10 mrad. It should be said, however, that in this analysis the receiver has been treated as a "black body": in real operative conditions the absorption capacity is lower and consequently also the useful power.

Therefore the use of an Innova 12m PDC with a degree of accuracy approaching 7 mrad seems to be a necessary condition to satisfy the requirements of the receiver-microturbine system.

On the other hand, should the available power be excessive, it would be possible to remove some mirrors from the dish reducing the interception area of the paraboloid. This action would obviously lead to a reduction of the concentration factor which however would remain higher than the required minimum.

Total tracking error (mrad)	7	10
External diameter (m)	11.73	
Shape ratio (F/D)	0.6	
Focus quote (m)	7.04	
Nominal aperture area (m ²)	108.1	
Aperture area reduction	0.89	
Effective aperture area (m ²)	96.14	
Flusso solare massimo (W/m ²)	800	
Intercepted solar power (W)	76942	
Concentrator reflection efficiency	0.95	
Solar energy on the focal plane (W)	73095	
Peak flux (kW/m ²)	4450	2390
Standard deviation (m)	0.06044	0.08241
Cavity window radius (m)	0.1	
Mean power density (kW/m ²)	2424	1692
Apparent absorbance (black body)	1	
Cavity emissivity (black body)	1	
Nominal operative temperature (°C)	750	
Cold tank temperature (°C)	25	
Focal plane incident power collection efficiency	0.75	0.52
Energy on the cavity window (W)	54498	38089
Concentration factor (suns)	2168	1515
Ideal maximum temperature (°C)	2079	1877
Window transmission efficiency	1	
Total absorbed energy (W)	54498	38089
Energy losses by radiation (W)	1952	
Conversion in useful power efficiency	0.964	0.948
Absorption efficiency	0.68	0.47
Net absorbed energy (W)	52546	36137
Carnot cycle efficiency	0.71	
Total efficiency	0.484	0.333

Table 10 – Optical and thermal performance for Innova 12m PDC

SIMUL-DISH: a portable ray tracing software for analytical dish simulation

(Marco Montecchi (ENEA))

In the previous chapters, optics and thermal-efficiency of dishes are discussed on the basis of some general assumptions. Particularly, the size of the solar spot concentrated at the focal plane is calculated by assuming that the statistical distribution of each important parameter is Gaussian. In particular two of them are very important: the divergence of solar radiation and the deviation of mirror shape from the ideal paraboloid. Indeed the Gaussian approach makes simpler the treatment by virtue of the property that linear combinations of normal (Gaussian) distributed variables is itself normal distributed.

On the other hand, in clear sky conditions, the angular distribution of solar radiation is much more close to rectangular than Gaussian function. Moreover, since the surface of the facets composing the reflector is continuous, the shape deviation in two points of the same facet is highly correlated. Therefore the deviation behaves as a continuous curve with features that are quite systematic for a given production batch of facets. Finally, for practical convenience, very often the mirrored surface of dishes is shaped as an annulus with a missing slice.

With the purposes of evaluating dish optical features in a more rigorous manner, the dedicated software SIMUL-DISH was developed. In the following its main features and some preliminary results are reported.

Software description

SIMUL-DISH is a cross-platform software (Linux, Mac, Windows), written in C++ with Qt graphical user interface (GUI). Experienced users can install it starting from the source codes; the others can install Virtual Box and then load the ready-to-use virtual machine file.

At startup, the GUI shown in Figure 44 pops up. In the left top box, titled “Concentrator”, curvature radius, inner and outer diameter of the mirrored annulus, and the angular extent of the dark slice can be set.

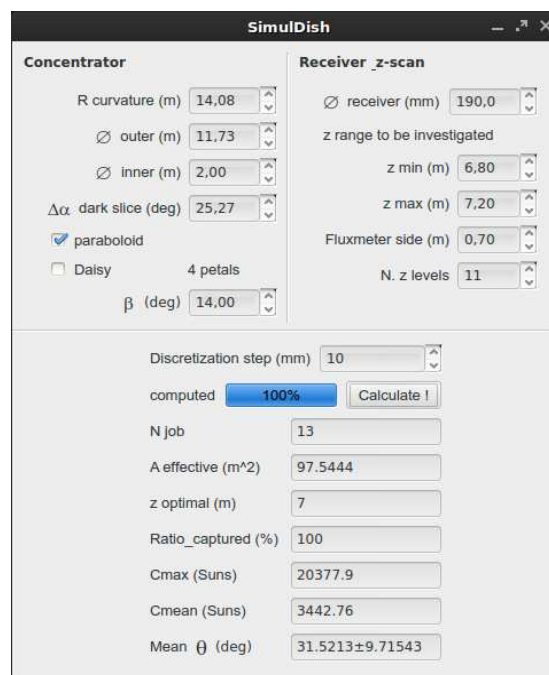


Figure 44 - GUI of SIMUL-DISH

The surface is assumed parabolic $z = r^2/(4f)$, with f focal distance, if “paraboloid” is checked; otherwise it is assumed spherical $z = 2f - \sqrt{4f^2 - r^2}$. In both the cases, the focal is set according to the relationship $f = R_{curvature}/2$. In the next future, experimental values of the surface achieved by in field measurement, in the form $x, y, z, \partial z/\partial x, \partial z/\partial y$, can be loaded by selecting a third option.

When “Daisy 4 petals” is checked, four replicas of the same annular concentrator are daisy-arranged around the z axis, with their optical axis aiming to the same point z_c , making the chosen β angle with \vec{z} .

In the right top box, titled “Receiver z-scan”, receiver (assumed circular) diameter, fluxmeter side, range and steps of z-scan can be set. As shown in Figure 45, the software “measures” the flux with a 201×201 virtual CCD. Its dimension is set to the “Fluxmeter side” value. The CCD rows (columns) are parallel to the X (Y) axis; its surface is parallel to the XY plane, and centred in $(0, 0, z)$. The flux measurement is repeated “N. z levels” times, with z ranging from “z min” to “z max”. Each time the flux ratio entering the receiver window, defined as ratio captured (RC), is computed. The criterion used to choice z-optimal value is where RC is maximum; that value is reported in the bottom box, together with: i) the effective capturing area viewed from the Sun; ii) maximum (Cmax) and mean (Cmean) value of the concentration factor expressed in Suns; iii) mean and standard deviation of the incidence angle of the reflected rays with the receiver window.

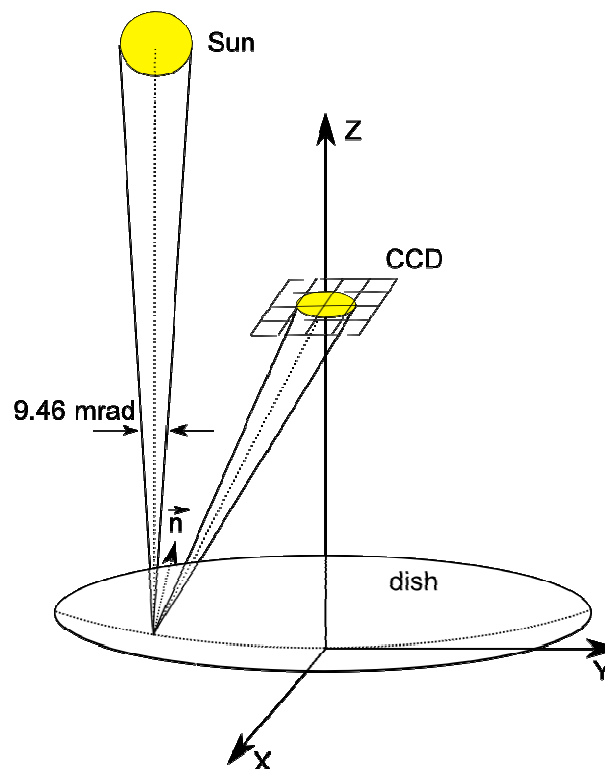


Figure 45 - Conceptual sketch of SIMUL-DISH working.

Except the progress bar, the numerical fields contained in the bottom box are filled/refreshed only at the job completion. At the same time four graphs will pop up (see Figure 46): 1) RC versus z , 2) mean and maximum C versus z , 3) flux contour map, and 4) contour map of the incidence angle distribution. In the flux contour map, the window is drawn as a white circle.

The numerical data are automatically stored in the “Dish” folder, in the two text files “fluxMap_job_#.txt” and IAD_job_#.txt; the latter is reserved to the incidence angle distribution, the other reports the CCD data achieved at the optimal z , soon after an header

summarizing configuration and parameters used in the computing. The job number “#” is automatically set to the first free lower number for which none file are present in the folder. The two contour map graphs are saved as jpeg images.

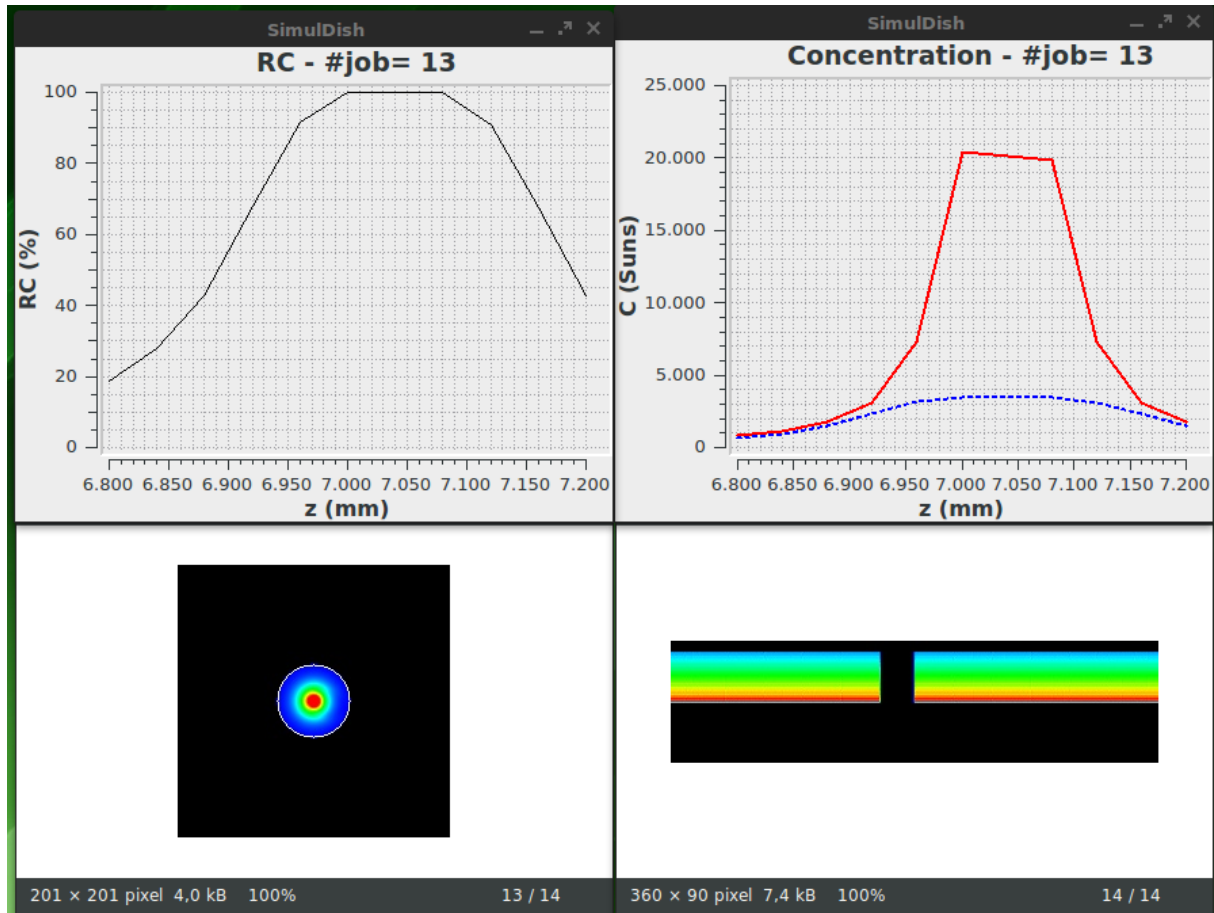


Figure 46 - Graphs automatically popped up on the desktop at the completion of the computing job.

The first parameter appearing in the bottom box (“Discretization step”) is very important because it is the step used in the numerical discretization of the mirror. When the software runs on quite power-limited computers, low discretization value may dramatically slow down the computing time; for that users are strongly recommended at the beginning to set discretization not less than 100 mm. Lower values should be only used later, for refining the results.

As shown in Fig. M4, the mirrored annulus is projected on the plane XY of the reference frame having the Z axis coincident to the paraboloid axis, and origin on the vertex. In that frame the projection is exactly circular; the diameter values of inner and outer circles are those selected in the GUI. Then the projection is divided in annulus sector having radial and angular size close to discretization step Δs .

As shown in Figure 47, in order to break down the computing-time, the ray tracing is dealt by considering only the ray travelling along the axis of the cone containing the direct solar radiation: the apex angle is set to typical divergence of solar radiation (9.46 mrad); the apex is put in the central point of the considered surface-element; the unit vector normal to the element-surface is obtained by the analytical equation of the surface; the reflection of the central ray is computed according to the laws of reflection. Around the cross-point of the reflected ray with the CCD plane, the elliptical intersection of the reflected solar beam is drawn; the counter of all the pixels internal to the ellipsoidal spot are added for the weight $S \cos(\theta_{inc})$, where S is the area of the surface-element, and θ_{inc} the incidence angle of the solar radiation impinging on it.

In the case of “Daisy” configuration, the achieved counting is suitably triplicated to take into account the contribution of the other three dishes.

The flux measurement is repeated at each one of the z plane selected in “z-scan”, and the results are recorded. Then the next surface-element is considered, and the computing procedure repeated.

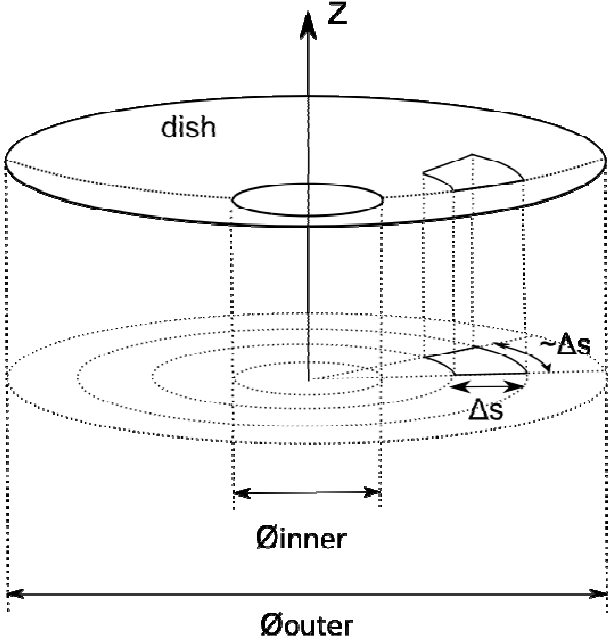


Figure 47 - The discretization is dealt on the projection of the dish onto the XY plane. The element is shaped as an annulus sector having radial and angular size close to the discretization step Δs .

Comparison between single and daisy-arrangement of dishes

The first application of SIMUL-DISH was the comparison between single and daisy-arrangement of four dishes. In both the cases the dish surface is set spherical, and the receiver window diameter is 190 mm. The single dish is mirrored for 11/12 of the circle-angle, thus the dark-slice angle is 30°, conversely the four dishes composing the daisy are fully mirrored (dark-slice angle 0°). Another difference is that single dish is not mirrored in the inner part ($\varnothing_{\text{inner}} = 1.2 \text{ m}$).

Table 11 resumes the characteristic parameters and the main results got in three jobs dealt for each one of the considered dish-configurations. Furthermore Figures 48-50 show flux distribution, RC and C, respectively.

job	$R_{\text{curvature}}$ (m)	\varnothing (m)	$A_{\text{effective}}$ (m ²)	Z_{receiver} (m)	RC(%)	C_{mean} (Suns)
Spherical_1 (11/12)	14	1.2 → 11.0	86.1	6.70	69.1	2104
Spherical_2 (11/12)	14	1.2 → 9.0	57.3	6.70	97.5	1982
Spherical_3 (11/12)	14	1.2 → 8.0	45.0	6.75	100.0	1592
Daisy_0 14.25°	12	4.0	48.7	5.15	87.2	1502
Daisy_1 14.00°	12	4.0	48.7	5.25	89.7	1547
Daisy_2 13.75°	12	4.0	48.8	5.35	86.1	1486

Table 11 – Comparison between single dish configuration and “daisy” configuration: characteristic parameters and results of some jobs

The first case of the single dish configuration (Spherical_1) has characteristics similar to those of 25 kW_e McDonnell Douglas dish. The low RC value means that the receiver window is not large enough to capture all the radiation, especially that reflected by the peripheral part of the dish; as matter of fact, as shown in the second case (Spherical_2), although the outer diameter is 2 m smaller, C_{mean} is just a bit lower, but RC is greatly higher. By reducing 1 m more the outer diameter (Spherical_3), all the radiation is captured (RC=100%), but C_{mean} is about ¾ of the first case.

Concerning the daisy-arrangement, the considered cases differ one to each other just for the angle made with the z axis, 14.25°, 14.0°, and 13.75°. With respect to the single-dish configuration, the daisy-arrangement is less efficient: RC is always lower than 90% and with the same concentration (Daisy_1 and Spherical_3) the encumbrance is much higher.

In any case, the RC behaviour is quite peaked, meaning that the distance of the receiver window from the vertex must be carefully adjusted.

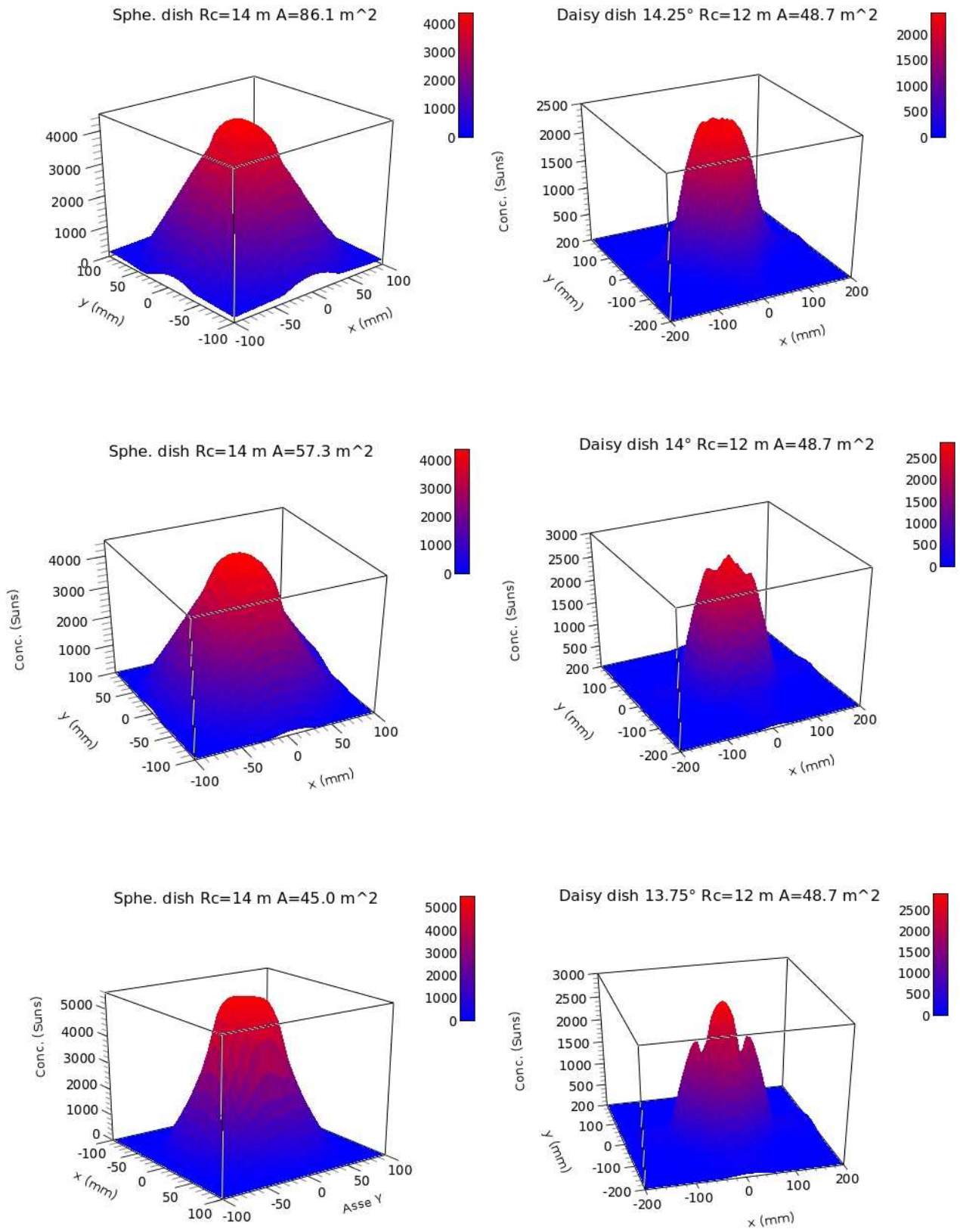


Figure 48 - Flux at z optimal.

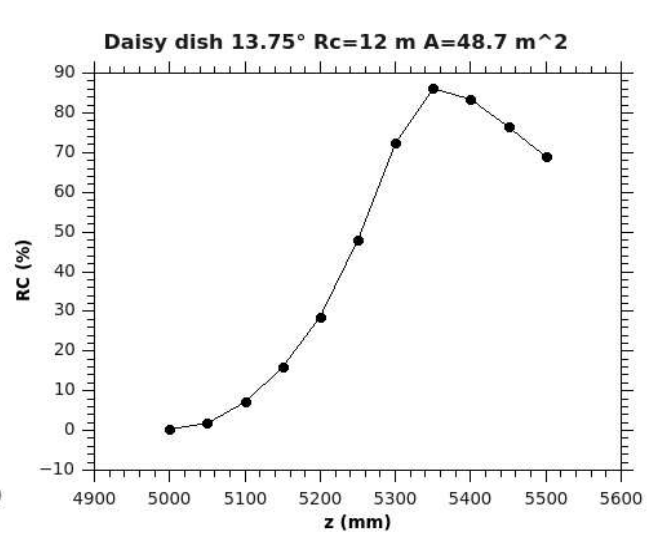
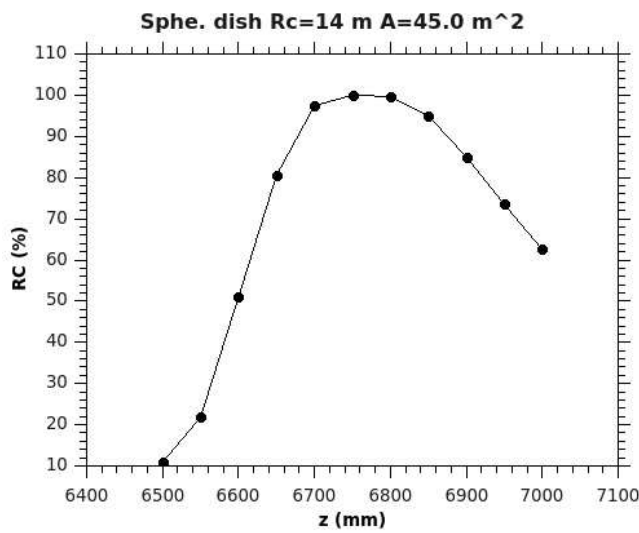
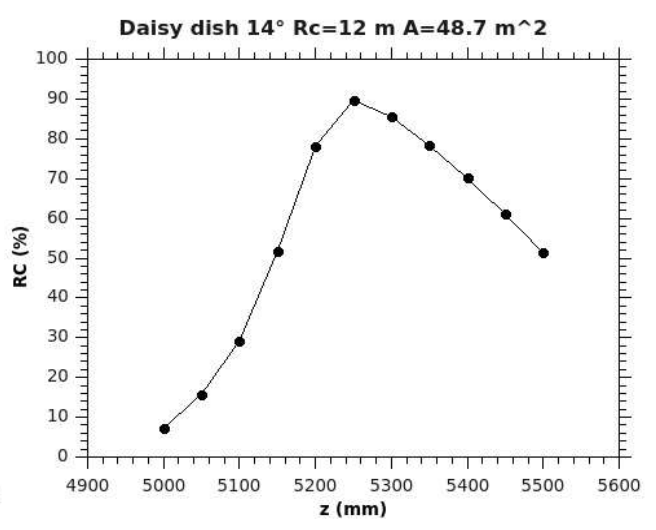
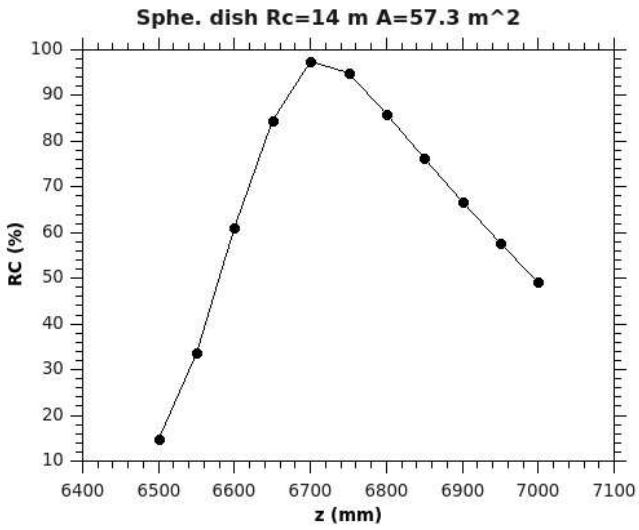
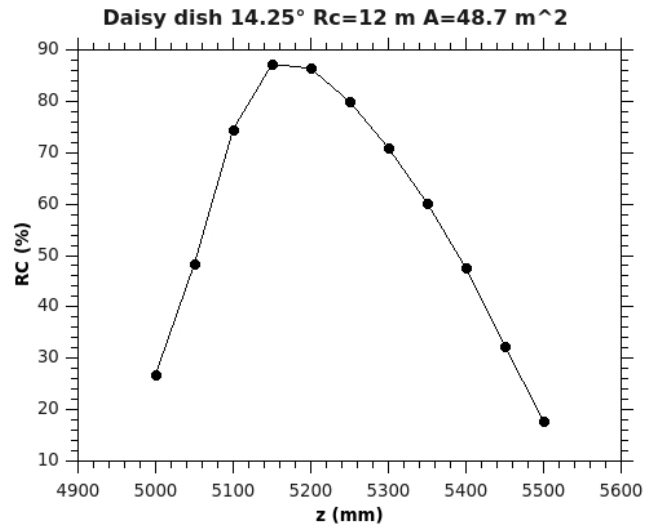
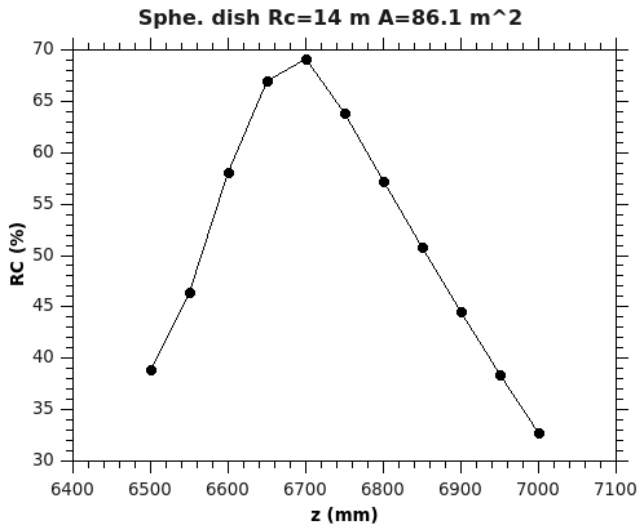


Figure 49 - RC versus z.

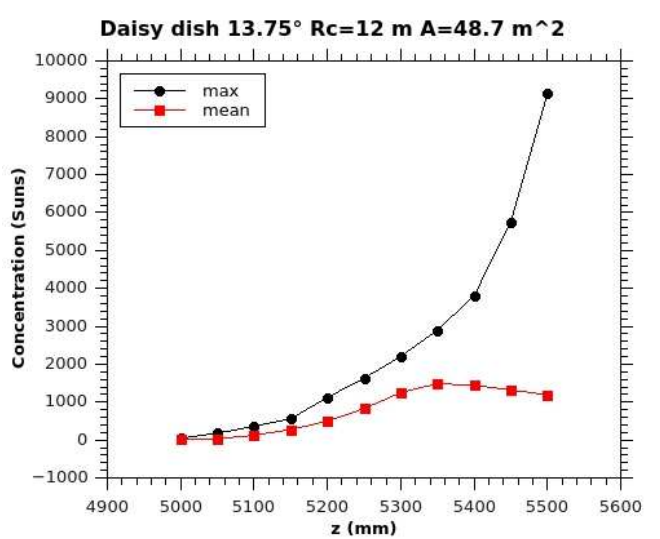
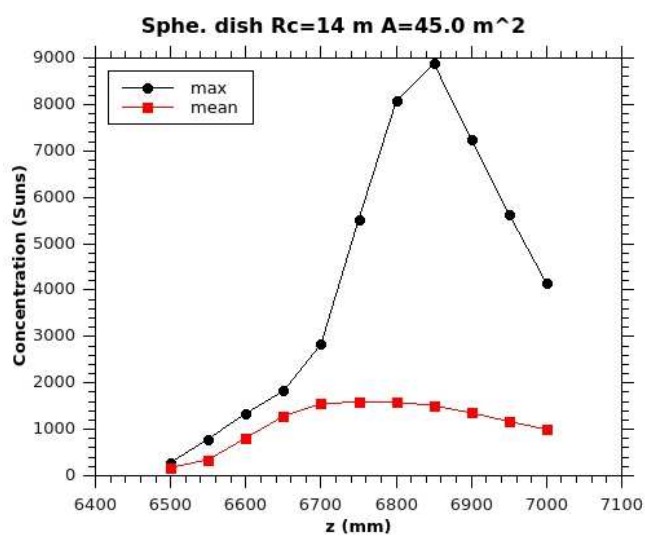
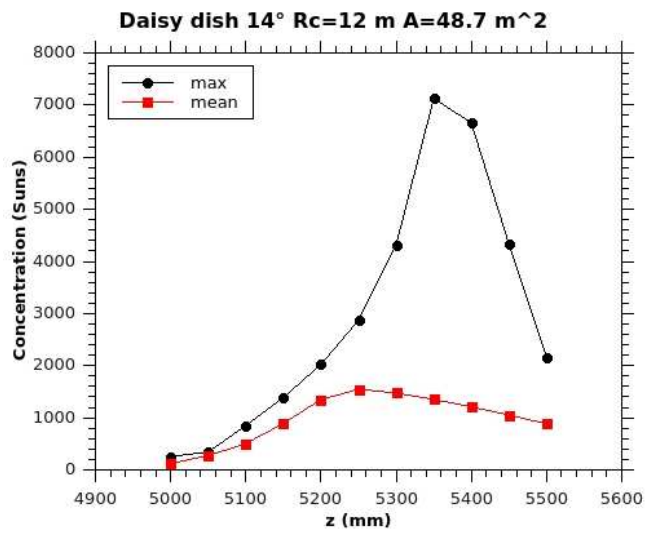
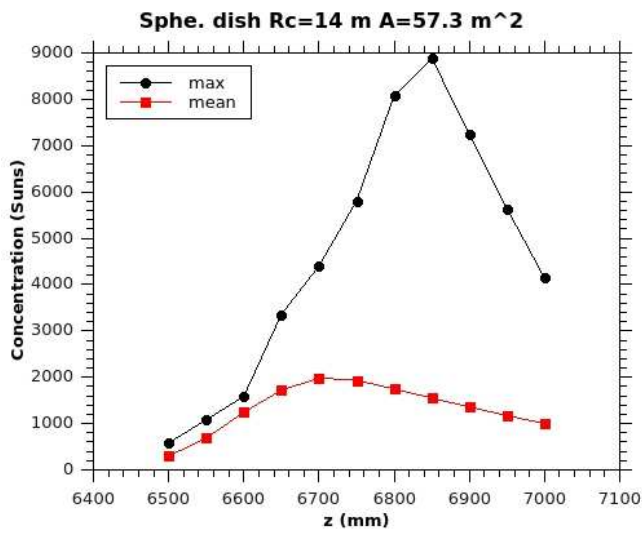
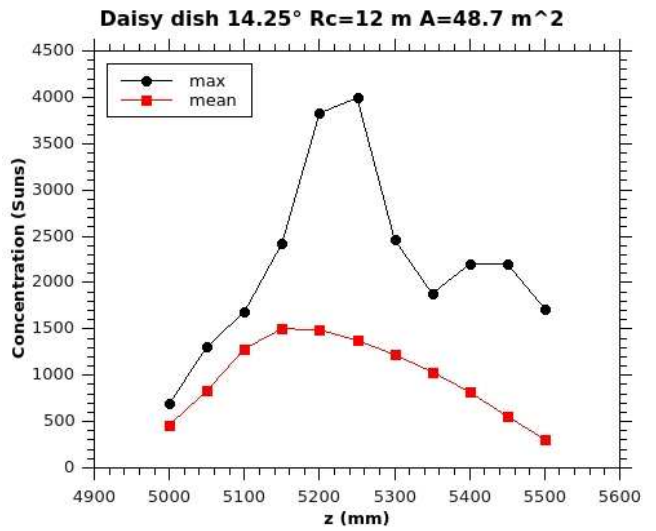
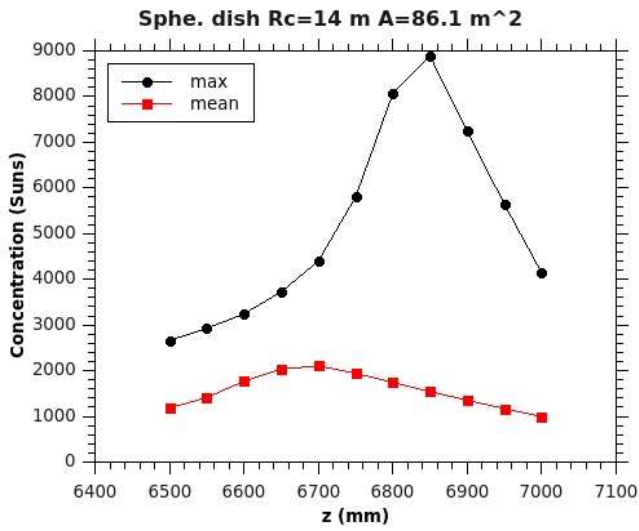


Figure 50 - Mean and maximum captured concentration versus z.

Simulation according to the latest OMSoP project outlining

The latest OMSoP project outlining adopts the single-dish configuration. Table 12 shows the dish parameters. The average angle of the dark-slice set in SIMUL-DISH is 25.27°.

Inner diameter (m)	2.00
Outer diameter (m)	11.73
Focal (m)	7.04 → curvature radius = 14.08 m
Missing inner facets	1.5
Installed inner facets	13
Missing outer facets	2
Installed outer facets	27

Table 12 - Parameters of the latest OMSoP dish candidate

Two jobs were launched; in the first the surface is assumed parabolic, in the other spherical. As shown in the left of Figure 51, RC is maximum at 7.05 m and 6.75 m for the parabolic and spherical surface, respectively. The shorter z-optimal value found for the spherical surface is due to the fact that the slope of the spherical surface, becomes greater than the parabolic one moving away from the vertex. As a consequence, the solar radiation is concentrated around the z axis at shorter distance from the vertex, and spread onto a wider spot as demonstrated by the graph of Cmean (Figure 51 right), and flux (Figure 52).

Concerning the mean incidence angle, the output is 31.52 ± 9.72 , and 33.18 ± 10.85 , respectively for parabolic and spherical case.

The flux is shown in Figure 53 as 3D plot, where: φ is the polar angle, and θ the incidence angle. Due to the symmetry of the reflector, the incidence angle is uniformly distributed versus φ , except in correspondence of the the dark slice. The distribution increases towards higher incidence angle, and reaches a peak close to $\theta \sim 50$ deg; that corresponds to the contribution of the peripheral annulus close to the outer border of the dish.

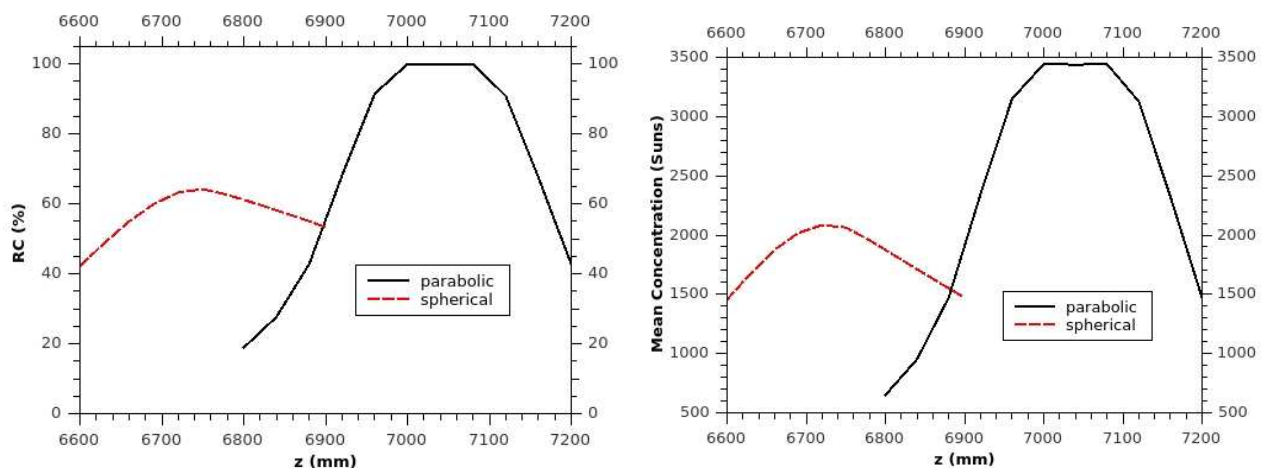


Figure 51 - Comparison of parabolic and spherical surface. On the left (right) z behaviour of RC (Cmean).

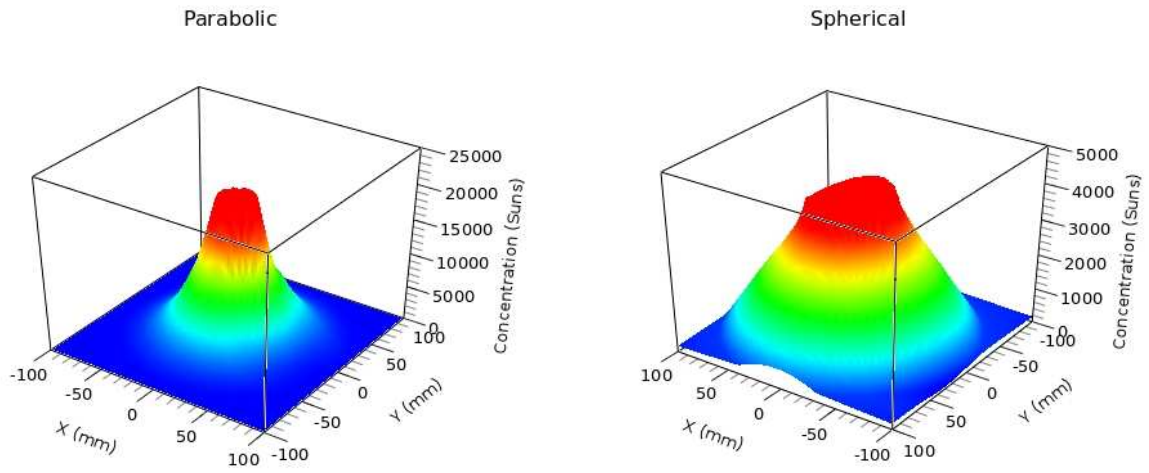


Figure 52 - Flux at z-optimal of parabolic (left) and spherical (right) dish.

Incidence angle distribution - parabolic

Incidence angle distribution - spherical

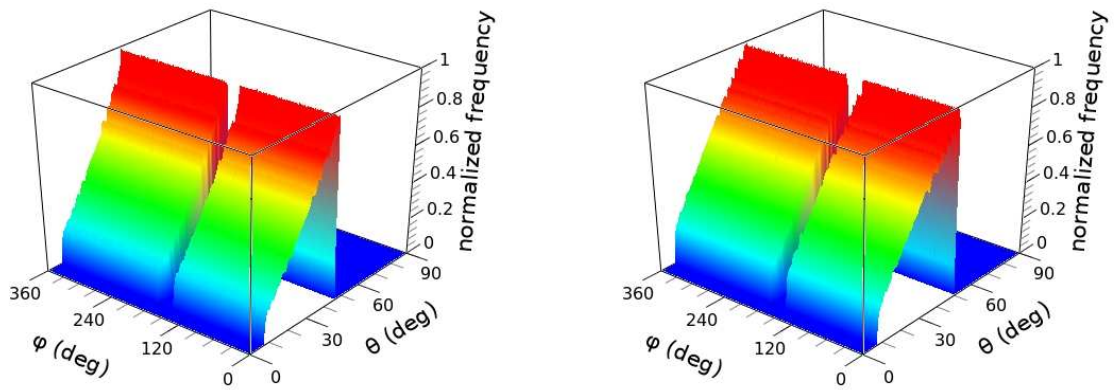


Figure 53 - Distribution of the incidence angle of the reflected rays on the window receiver of the dish with characteristic shown on Table 11 with parabolic (left) or spherical (right) surface.

Wind loads analysis

(Adio Miliozzi (ENEA))

Scope of the present work is to evaluate the wind loads acting on the 12m parabolic dish collector (PDC) proposed by Innova for the demonstration task of the project. This type of collector, indeed, is heavily exposed to environmental conditions and, in particular, to the wind actions.

Codes and Standards

Main references, in Europe, to determine the wind actions on a structure are the following Eurocodes [1,2]

- Eurocode 1: Basis of design and actions on structures. Part 2-4: Wind actions, CEN, ENV 1991-2-4, 1994.
- Eurocode 1: Actions on structures - General actions. Part 1-4: Wind actions, CEN, EN 1991- 1-4, 2005.

The Italian codes and standards are directly derived from the previous Eurocodes [3,4]:

- Norme tecniche per le costruzioni, D.M. 14 gennaio 2008.
- Istruzioni per la valutazione delle azioni e degli effetti del vento sulle costruzioni - CNR-DT 207/2008

Other references, useful to support this evaluation can be [5,6,7]:

- G. M. Giannuzzi, C. E. Majorana, A. Miliozzi, V.A. Salomoni, D. Nicolini, Structural Design Criteria for Steel Components of Parabolic-Trough Solar Concentrators, Journal of Solar Energy Engineering, NOVEMBER 2007, Vol. 129 / 383
- Miliozzi, G.M. Giannuzzi, D. Nicolini, Valutazione dell'azione del vento su di un concentratore solare parabolico lineare, ENEA Technical Report RT/TER/13/2007
- F. Crobu, Analisi numerica e sperimentale dell'azione del vento su concentratori solari parabolici, Tesi Università di Perugia, 2005

Definition of the wind actions

Wind loads (forces and moments) acting on a PDC are defined in a 3D space as shown in Figure 54.

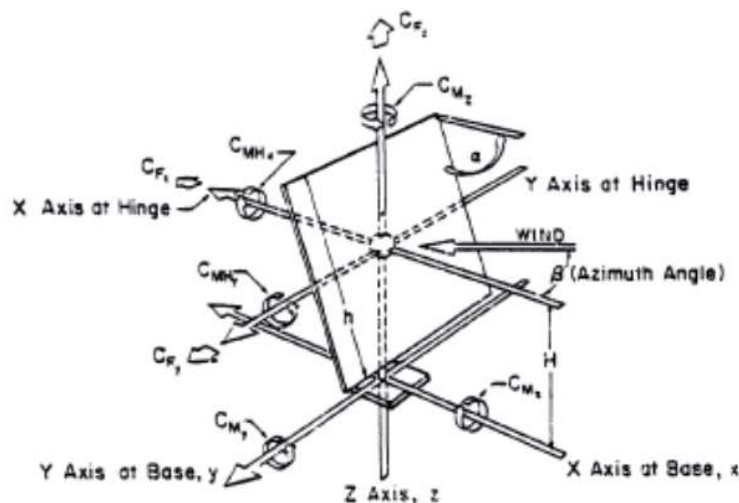


Figure 54- Coordinate system for heliostats and parabolic dish collectors [8].

Wind loads will be evaluated as a function of the peak dynamic pressure of the wind, the main dimension and the aerodynamic coefficients of the PDC in the following way:

$$F_x = C_{Fx} \cdot q \cdot A$$

$$F_y = C_{Fy} \cdot q \cdot A$$

$$F_z = C_{Fz} \cdot q \cdot A$$

$$M_{Hx} = C_{MHx} \cdot q \cdot A \cdot D$$

$$M_{Hy} = C_{MHy} \cdot q \cdot A \cdot D$$

$$M_z = C_{Mz} \cdot q \cdot A \cdot D$$

where D and A are the PDC diameter and aperture area, q is the peak dynamic pressure, C is the aerodynamic coefficient, H is the reference quote of the structure.

The peak dynamic pressure q can be calculated, as stated in [1,2,5], as a function of the wind speed, the site characteristics and the reference quote of the structure.

The aerodynamic coefficients C are function of the wind direction (β , azimuth angle) and the PDC elevation (α). These coefficients are provided, for common structures, directly by the codes and standards but, for not common structures (our case) they must be evaluated by experimental tests or numerical calculations.

Aerodynamic coefficients: CNR-DT207/2008

CNR-DT207/2008 is the more updated Italian standard devoted to the determination of the wind actions on buildings and structures. Over the general rules, in analogy to what is reported in the section 0, for the calculation of the wind actions, the aerodynamic coefficients for parabolic antennas are evaluated in Appendix G.8.2 of the standard. These type of objects are very close to the parabolic solar collectors and can be used as a reference for our analysis. The evaluation of the coefficients is performed in a simplified manner imagining that the wind impacts on the paraboloid with a uniform distribution of wind speed. In this way there is always a condition of symmetry with respect to the plane identified by the axis coincident with the wind direction and the axis of the paraboloid. The problem is reduced to a two-dimensional case and the aerodynamic coefficients are only function of the angle α and the shape of the parabola (f/D ratio, where f is the focal length and D the diameter of the paraboloid). The reference scheme is shown in Figure 55.

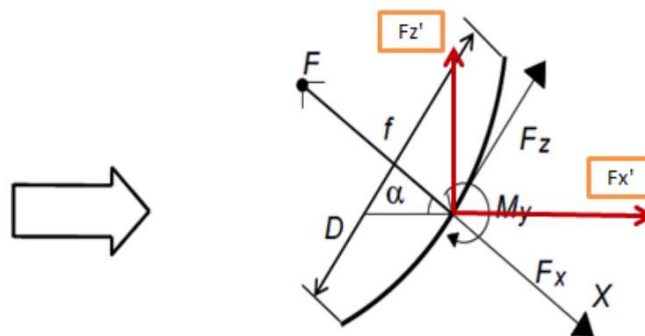


Figure 55- Coordinate system for PDC in CNR-DT-207 standard.

The coefficient of the aerodynamic force parallel to the axis of the paraboloid (C_{Fx}) depends on the angle α which defines the inclination on the horizontal axis of the paraboloid and the ratio f/D. This coefficient is represented in Figure 56 and can be calculated from the following relations:

$$c_{FX} = -0,0521 \cdot \alpha + 5,03$$

$$-0,7 \leq c_{FX} \leq 1,8$$

$$-1,1 \leq c_{FX} \leq 1,5$$

$$f/D = 0,2$$

$$f/D = 1,0$$

where α is expressed in degree (°).

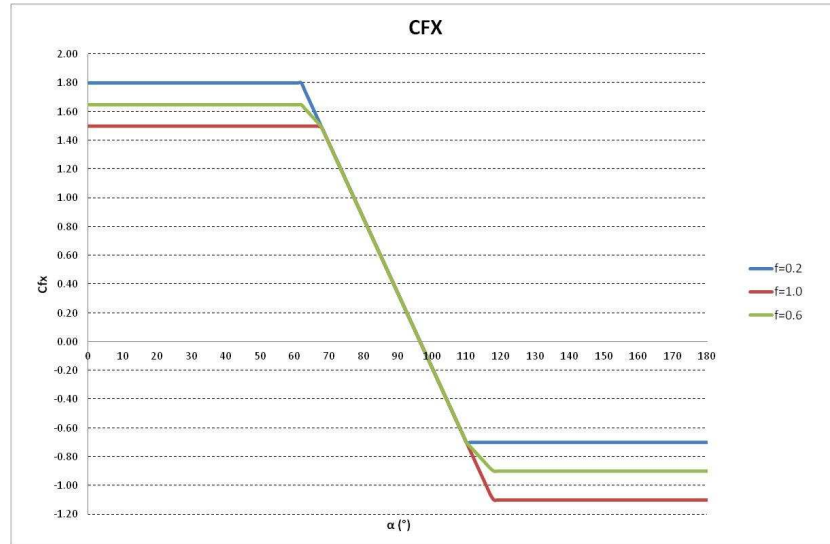


Figure 56- C_{FX} aerodynamic coefficient

For f/D ratios between 0.2 and 1.0 it is possible to linearly interpolate the values given in Figure 56. For values external to the range $f/D=0.2-1.0$, it is not possible to adopt the aerodynamic coefficient C_{FX} values given in Figure 56.

The coefficient of the aerodynamic force perpendicular to the axis of the paraboloid C_{FZ} depends on the angle α and on the ratio f/D (Figure 55). This coefficient is represented in Figure 57 and can be calculated from the following relations:

$$\begin{array}{ll}
 c_{FZ} = 0,05 & \alpha \leq 75^\circ \\
 c_{FZ} = 0,01 \cdot \alpha - 0,7 & 75^\circ < \alpha \leq 90^\circ \\
 c_{FZ} = 0,0023 \cdot \alpha - 0,0025 & 90^\circ < \alpha \leq 130^\circ \\
 c_{FZ} = -0,006 \cdot \alpha + 1,08 & 130^\circ < \alpha \leq 180^\circ
 \end{array}
 \quad f/D = 0,2$$

$$\begin{array}{ll}
 c_{FZ} = -0,1 & \alpha \leq 60^\circ \\
 c_{FZ} = 0,005 \cdot \alpha - 0,4 & 60^\circ < \alpha \leq 80^\circ \\
 c_{FZ} = 0,002 \cdot \alpha - 0,16 & 80^\circ < \alpha \leq 130^\circ \\
 c_{FZ} = -0,002 \cdot \alpha + 0,36 & 130^\circ < \alpha \leq 180^\circ
 \end{array}
 \quad f/D = 1,0$$

where α is expressed in degree (°).

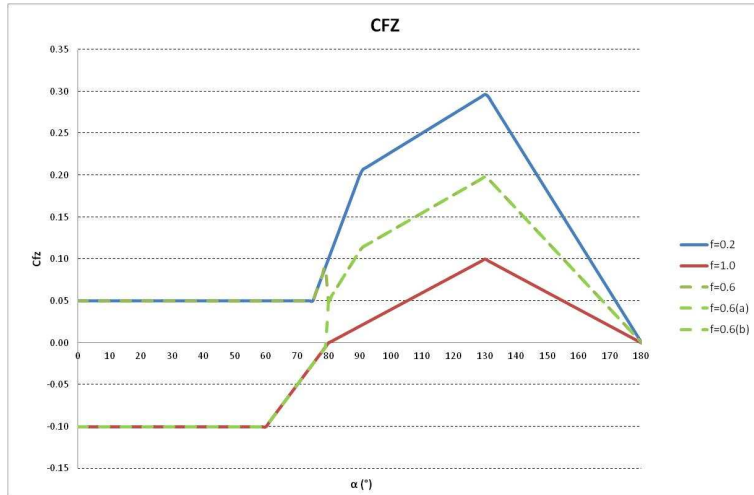


Figure 57- C_{FZ} aerodynamic coefficient

For f/D ratios between 0.2 and 1.0 it is possible to linearly interpolate the values given in Figure 57, provided that these have the same sign; otherwise both values of opposite sign can be considered. For values external to the range $f/D=0.2-1.0$, it is not possible to adopt the C_{FZ} aerodynamic coefficient given in Figure 57.

The moment coefficient C_{MY} is defined by the relation: $C_{MY} = C_{FZ} \frac{x_{FZ}}{D}$ (Figure 58), where x_{FZ} is the eccentricity of the transversal force given in Figure 59.

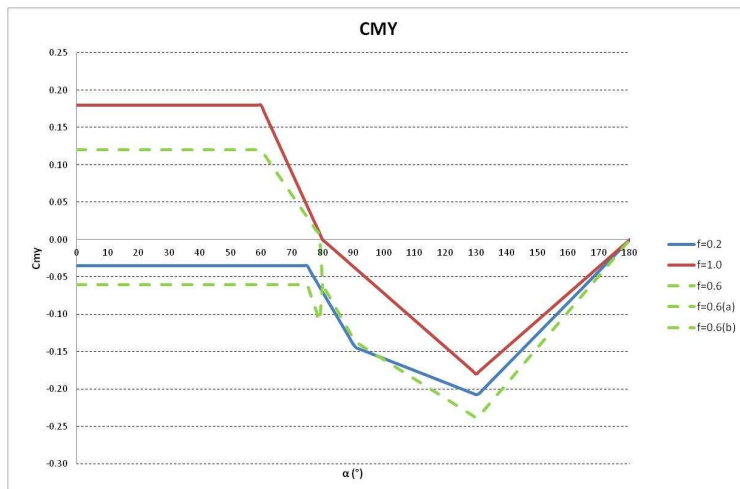


Figure 58- C_{MY} aerodynamic coefficient

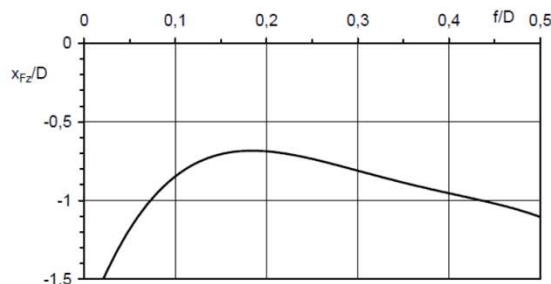


Figure 59- Eccentricity of the transversal force FZ

In Figure 56, Figure 57 and Figure 58, a green line, representative of the aerodynamic coefficients for the PDC most common case $f/D=0.6$, has been reported. In the previous analysis, a coordinate system fixed to the parabola has been adopted. In the PDC case it is better, in order to facilitate the comparison with other methods, to adopt a new coordinate system with the x axis parallel to the wind direction (red lines in Figure 55). In this case the new aerodynamic coefficients are shown in the following figures.

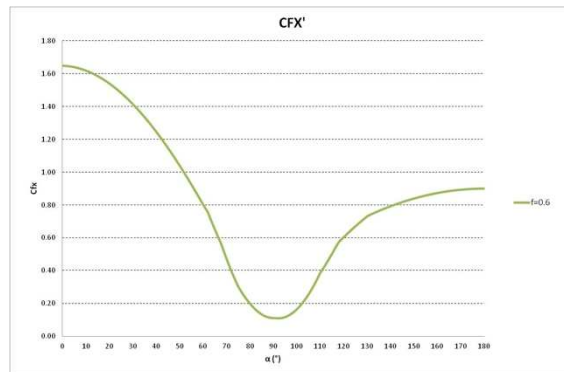


Figure 60- C_{FX} aerodynamic coefficient in wind coordinates system

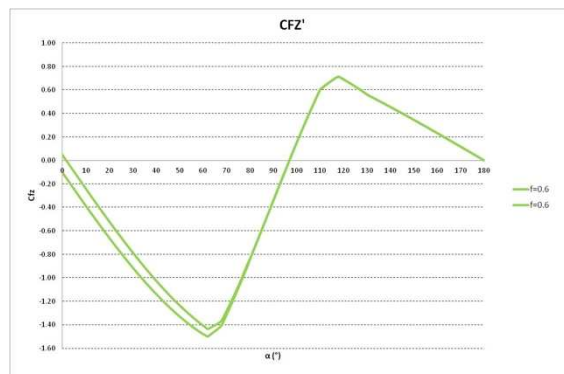


Figure 61 - C_{FZ} aerodynamic coefficient in wind coordinates system

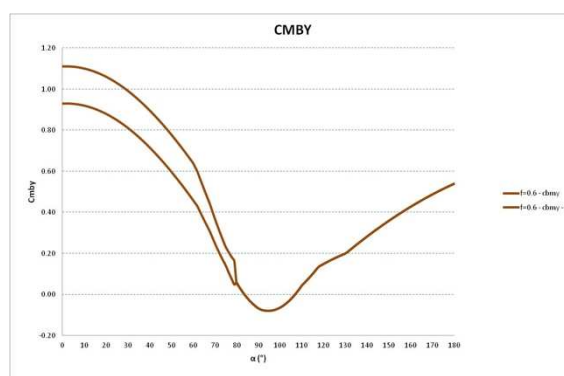


Figure 62 - Moment aerodynamic coefficient (C_{MBY}) at PDC base with 5m diameter (D) and 3m high (H)

Aerodynamic coefficients: Wind tunnel experimental tests

Dr. Peterka and al. have conducted, in the years from 1988 and 1992 [8-10] some wind tunnel experimental tests on heliostats and PDCs (Figure 63), finalized at evaluating the aerodynamic coefficients of this type of structures.

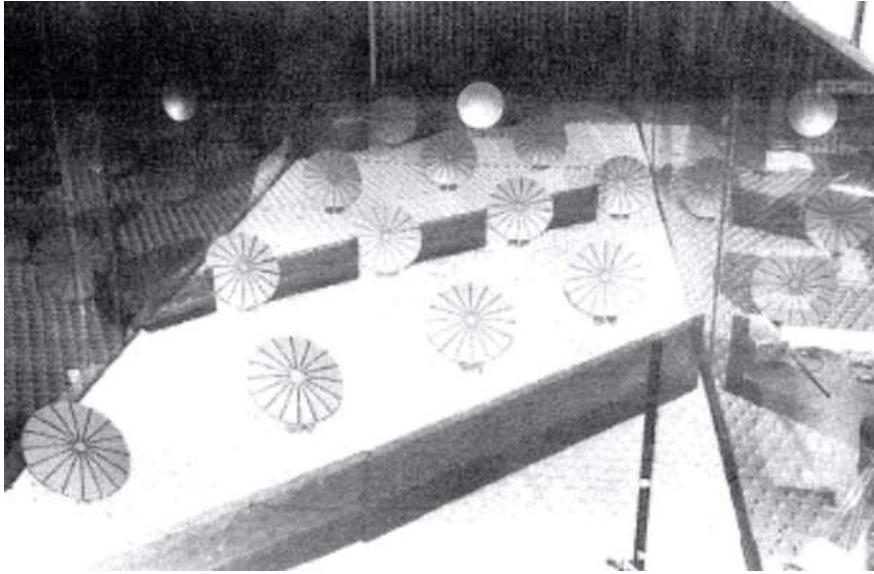


Figure 63 - In-field Study of Parabolic Dishes

From Figure 64 to Figure 68 all main results obtained in the wind tunnel experimental tests (drag, lift and lateral force and torque and hinge moment coefficients) are summarized.

The coordinate system considered in these figures is the same shown in Figure 54. The shape factor (f/D) of the parabolic dish is about 0.6.

In each figure the trend of the aerodynamic coefficients as a function of the elevation angle for different values of the azimuth angle between 0° and 90° s represented.

The experimental results are also shown from Table 13 to Table 17.

Instead, in Figure 69 and Figure 70 the same coefficients in the specific case of 0° azimuth angle are reported. This condition should be substantially similar to that reported by Italian standards. In this case, the value of the bending moment at the base of a PDC having 5m diameter and 3m hinge height is also evaluated.

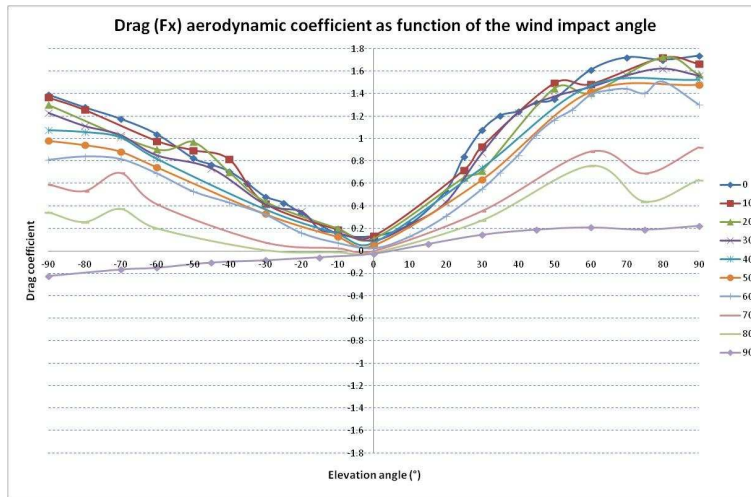


Figure 64 – Drag force aerodynamic coefficients (Peterka.)

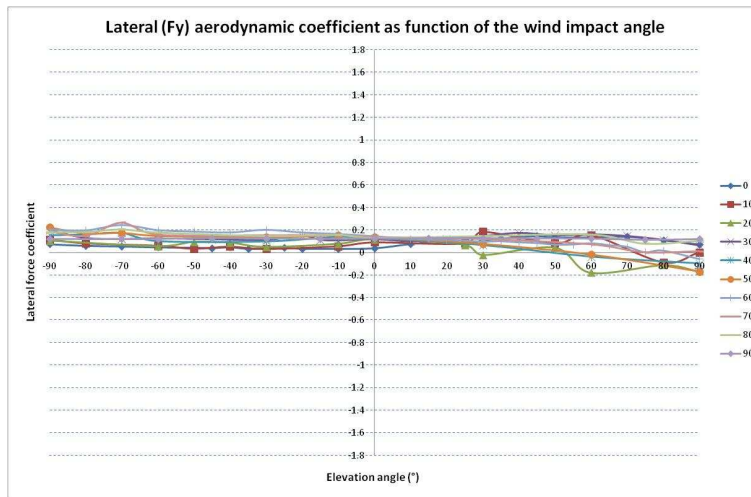


Figure 65 - Lateral force aerodynamic coefficients (Peterka.)

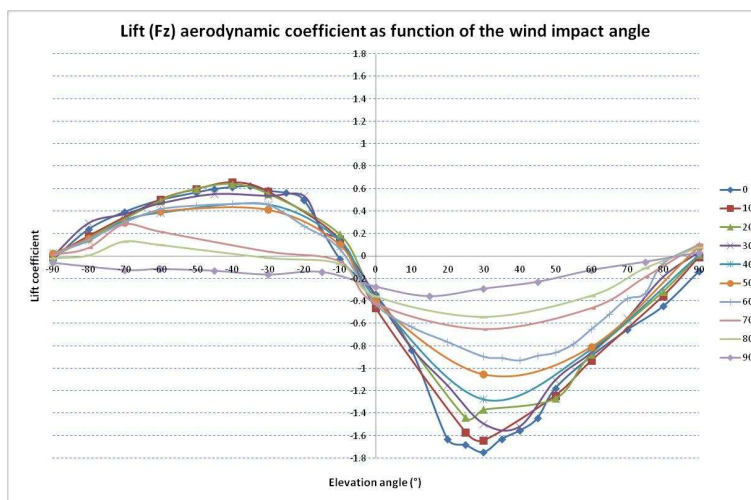


Figure 66 - Lift force aerodynamic coefficients (Peterka.)

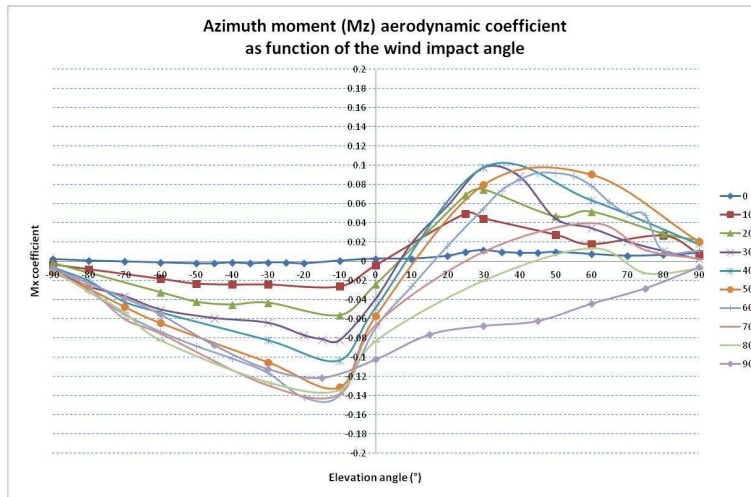


Figure 67 - Azimuth moment aerodynamic coefficients (Peterka.)

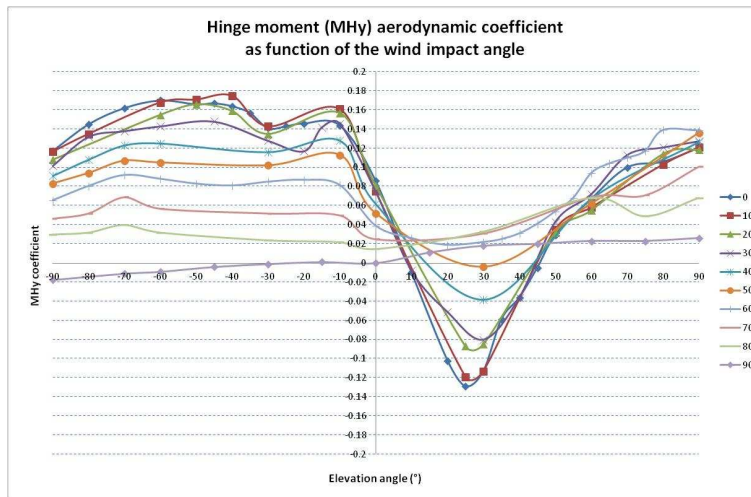


Figure 68 – Hinge moment aerodynamic coefficients (Peterka.)

CFx	Wind																
	Elev	0	10	15	20	30	40	45	50	55	60	65	70	75	80	85	90
90	1.7395	1.6685		1.5735	1.562	1.5285	1.4795	1.4825	1.391	1.303	1.324	0.926		0.634			0.224
80	1.703	1.723		1.728	1.625					1.507							
75										1.4025		0.692		0.44			0.191
70	1.725				1.564					1.443							
65										1.43							
60	1.612	1.487		1.411	1.46	1.475	1.426	1.419	1.415	1.388	1.185	0.887		0.757			0.21
55										1.257							
50	1.353	1.495		1.45	1.377					1.166							
45	1.323						1.119			1.034							0.191
40	1.244				1.233					0.852							
35	1.205									0.698							
30	1.076	0.931		0.714	0.874	0.742	0.652	0.636	0.548	0.552	0.454	0.357		0.273			0.145
25	0.842	0.721		0.654													
20	0.535				0.435					0.31							
15																	0.063
10	0.238				0.235					0.129							
0	0.132	0.133		0.109	0.095	0.075	0.05	0.051	0.033	0.025	0.009	0.001		-0.015			-0.023
-10	0.154	0.191		0.201	0.163	0.155		0.129		0.073		0.026		-0.009			
-15					0.196												-0.055
-20	0.337		0.372		0.354		0.299			0.1615			0.072				
-25	0.43																
-30	0.485	0.424		0.44	0.418	0.374		0.332		0.326		0.077		0.009			-0.082
-35	0.605																
-40	0.71	0.819		0.705						0.432							
-45	0.771				0.739												-0.102
-50	0.828	0.899		0.973						0.532							
-60	1.041	0.981		0.906	0.854	0.825		0.748		0.692		0.419		0.203			-0.148
-70	1.177				1.034	1.015		0.887		0.819		0.697		0.376			-0.164
-80	1.28	1.258			1.115	1.063		0.945		0.8415		0.535		0.259			
-90	1.3925	1.368		1.3025	1.232	1.079		0.9825		0.812		0.5935		0.346	0.132		-0.2215

Table 13 – C_{FX} aerodynamic coefficients

CFy	Wind																
	Elev	0	10	15	20	30	40	45	50	55	60	65	70	75	80	85	90
90	0.075	0.0045		-0.1655	0.0625	-0.0955	-0.209	-0.166	-0.1185	-0.0545	0.034	0.0125			0.108		0.122
80	0.113	-0.084		-0.11	0.114					0.02							
75										0.0055		0.002		0.082			0.116
70	0.144				0.148					0.054							
65										0.069							
60	0.138	0.158		-0.176	0.164	-0.035	-0.071	-0.015	0.045	0.085	0.089	0.074		0.164			0.126
55										0.074							
50	0.14	0.086		0.044	0.155					0.073							
45	0.15						0.016			0.087							0.129
40	0.14				0.176					0.093							
35	0.126									0.103							
30	0.111	0.187		-0.02	0.146	0.068	0.086	0.079	0.108	0.1	0.129	0.121		0.149			0.131
25	0.078	0.083		0.07													
20	0.109				0.123					0.114							
15																	0.131
10	0.079				0.1					0.124							
0	0.041	0.093		0.117	0.12	0.128	0.135	0.138	0.146	0.147	0.144	0.14		0.134			0.126
-10	0.036	0.059		0.079	0.108	0.141		0.155		0.167		0.157		0.16			
-15					0.114												0.124
-20	0.037		0.075		0.15		0.172			0.1795			0.18				
-25	0.045																
-30	0.041	0.035		0.051	0.112	0.1		0.139		0.204		0.156		0.15			0.129
-35	0.036																
-40	0.049	0.055		0.089						0.18							
-45	0.043				0.119												0.131
-50	0.046	0.037		0.096						0.188							
-60	0.049	0.063		0.057	0.126	0.103		0.151		0.201		0.161		0.181			0.124
-70	0.057				0.121	0.176		0.177		0.246		0.269		0.209			0.121
-80	0.063	0.085			0.13	0.162		0.172		0.1985		0.151		0.186			
-90	0.0765	0.1195		0.107	0.2025	0.155		0.226		0.206		0.1885		0.186	0.163		0.1235

Table 14 – C_{FY} aerodynamic coefficients

CFz	Wind																
	Elev	0	10	15	20	30	40	45	50	55	60	65	70	75	80	85	90
90	-0.1355	-0.0065		0.0135	0.0975	0.0135	0.0525	0.0875	0.1155	0.103	0.088	0.109		0.079			0.033
80	-0.446	-0.354		-0.315	-0.184					-0.065							
75										-0.331		-0.187		-0.107			-0.05
70	-0.656				-0.554					-0.378							
65										-0.517							
60	-0.89	-0.931		-0.872	-0.858	-0.827	-0.8845	-0.807	-0.752	-0.65	-0.634	-0.464		-0.353			-0.124
55										-0.781							
50	-1.176	-1.241		-1.266	-1.104					-0.857							
45	-1.443						-1.152			-0.885							-0.229
40	-1.553				-1.519					-0.926							
35	-1.627									-0.904							
30	-1.744	-1.643		-1.366	-1.491	-1.273	-1.166	-1.05	-0.957	-0.891	-0.814	-0.651		-0.541			-0.29
25	-1.679	-1.567		-1.435													
20	-1.627				-1.151					-0.761							
15																	-0.357
10	-0.835				-0.817					-0.628							
0	-0.341	-0.462		-0.357	-0.349	-0.371	-0.395	-0.401	-0.412	-0.425	-0.393	-0.421		-0.357			-0.272
-10	-0.022	0.15		0.194	0.139	0.142		0.104		0.0655		-0.047		-0.069			
-15					0.225												-0.14
-20	0.501		0.556		0.54		0.443			0.2695			0.105				
-25	0.563																
-30	0.585	0.579		0.557	0.54	0.463		0.415		0.458		0.042		-0.015			-0.164
-35	0.624																
-40	0.616	0.66		0.643						0.464							
-45	0.599				0.555												-0.13
-50	0.568	0.598		0.6						0.451							
-60	0.501	0.505		0.494	0.472	0.39		0.401		0.417		0.22		0.1			-0.115
-70	0.395				0.377	0.32		0.302		0.302		0.287		0.132			-0.122
-80	0.24	0.18			0.296	0.141		0.155		0.147		0.075		0.006			
-90	-0.033	-0.008		-0.0055	-0.0035	0.029		0.023		0.01		0.0115		-0.019	-0.027		-0.0585

Table 15 – C_{FZ} aerodynamic coefficients

CMx	Wind																
	Elev	0	10	15	20	30	40	45	50	55	60	65	70	75	80	85	90
90	0.009	0.008		0.022	0.0025	0.018	0.0295	0.021	0.0185	0.011	0.001	0.003		-0.0075			-0.006
80	0.007	0.027		0.029	0.011					0.011							
75										0.0485		0.012		-0.012			-0.028
70	0.006				0.021					0.05							
65										0.062							
60	0.008	0.018		0.052	0.035	0.064	0.107	0.091	0.088	0.079	0.072	0.04		0.014			-0.044
55										0.089							
50	0.01	0.028		0.047	0.045					0.092							
45	0.009						0.117			0.092							-0.062
40	0.009				0.089					0.085							
35	0.01									0.074							
30	0.012	0.045		0.075	0.098	0.098	0.09	0.08	0.067	0.055	0.039	0.01		-0.02			-0.067
25	0.01	0.05		0.069													
20	0.006				0.058					0.016							
15																	-0.076
10	0.003				0.019					-0.026							
0	0.003	-0.004		-0.024	-0.039	-0.048	-0.06	-0.057	-0.056	-0.069	-0.071	-0.066		-0.083			-0.102
-10	0.001	-0.026		-0.056	-0.082	-0.103		-0.131		-0.139		-0.138		-0.134			
-15					-0.081												-0.121
-20	-0.002		-0.041		-0.077		-0.108			-0.1415			-0.145				
-25	-0.001																
-30	-0.001	-0.024		-0.043	-0.064	-0.082		-0.105		-0.116		-0.129		-0.126			-0.112
-35	-0.002																
-40	-0.001	-0.024		-0.045						-0.101							
-45	-0.002				-0.059												-0.087
-50	-0.002	-0.023		-0.042						-0.088							
-60	-0.001	-0.018		-0.032	-0.05	-0.053		-0.064		-0.073		-0.075		-0.082			-0.055
-70	0				-0.036	-0.042		-0.047		-0.055		-0.06		-0.053			-0.038
-80	0.001	-0.008			-0.026	-0.02		-0.028		-0.031		-0.027		-0.031			
-90	0.0025	-0.003		-0.0015	-0.0095	-0.006		-0.011		-0.009		-0.007		-0.0085	-0.007		-0.007

Table 16 – C_{MZ} aerodynamic coefficients

CMY	Wind																
	Elev	0	10	15	20	30	40	45	50	55	60	65	70	75	80	85	90
90	0.1205	0.121		0.1185	0.1275	0.1265	0.131	0.136	0.1365	0.1385	0.144	0.101		0.068			0.026
80	0.106	0.103		0.114	0.121					0.139							
75										0.117		0.071		0.049			0.023
70	0.1				0.113					0.11							
65										0.104							
60	0.067	0.058		0.055	0.072	0.067	0.0565	0.062	0.071	0.094	0.081	0.069		0.068			0.023
55										0.068							
50	0.029	0.035		0.032	0.043					0.054							
45	-0.005						-0.001			0.041							0.02
40	-0.036				-0.036					0.031							
35	-0.059									0.025							
30	-0.113	-0.113		-0.085	-0.08	-0.038	-0.02	-0.004	0.006	0.022	0.025	0.031		0.033			0.018
25	-0.129	-0.119		-0.087													
20	-0.102				-0.051					0.019							
15																	0.011
10	-0.01				-0.008					0.026							
0	0.086	0.075		0.081	0.075	0.062	0.061	0.052	0.04	0.039	0.031	0.025		0.015			0
-10	0.144	0.161		0.157	0.146	0.128		0.113		0.0815		0.05		0.022			
-15					0.142												0.001
-20	0.146		0.159		0.117		0.089			0.087			0.041				
-25	0.143																
-30	0.141	0.143		0.135	0.128	0.116		0.102		0.085		0.052		0.024			-0.001
-35	0.157																
-40	0.164	0.175		0.159						0.081							
-45	0.167				0.148												-0.004
-50	0.166	0.171		0.166						0.083							
-60	0.17	0.168		0.155	0.143	0.125		0.105		0.088		0.057		0.032			-0.009
-70	0.162				0.138	0.123		0.107		0.092		0.069		0.04			-0.011
-80	0.145	0.135			0.132	0.108		0.094		0.0805		0.052		0.032			
-90	0.117	0.1165		0.108	0.1015	0.091		0.083		0.0655		0.0465		0.03	0.014		-0.0175

Table 17 – C_{MHY} aerodynamic coefficients

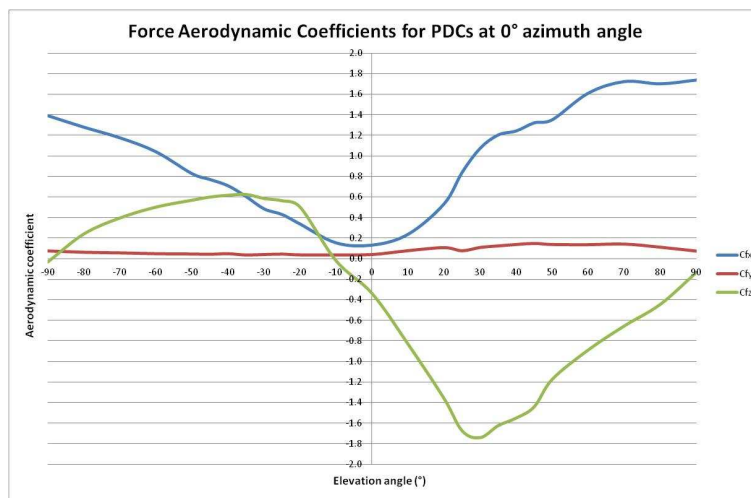


Figure 69 – Force aerodynamic coefficients for 0° azimuth angle

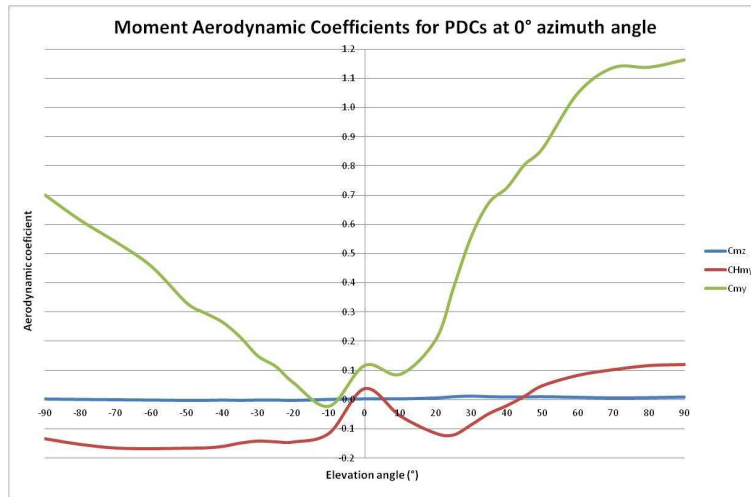


Figure 70 - Moment aerodynamic coefficients for 0° azimuth angle

Aerodynamic coefficients: methods comparison

In a previous paragraph the aerodynamic coefficients of a PDC referring to current Italian legislation [1,2,3,4] have been obtained and, in particular, the CNR-DT 207/2008. These values have been reported to a fixed reference system, whose x-axis is parallel to the ground and oriented according to the wind direction, as shown in Figure 60 and Figure 61.

As a second step, the aerodynamic coefficients obtained through a series of tests in the wind tunnel have been extracted from NREL documents [8,9,10]. The values of these coefficients are shown from Figure 64 to Figure 68, and, in the case of the azimuth angle of the wind equal to 0°, in Figure 69 and Figure 70.

From Figure 71 to Figure 74 the data obtained by the two evaluations, the standards and the experimental one, have been compared in order to verify the compatibility of the two methods.

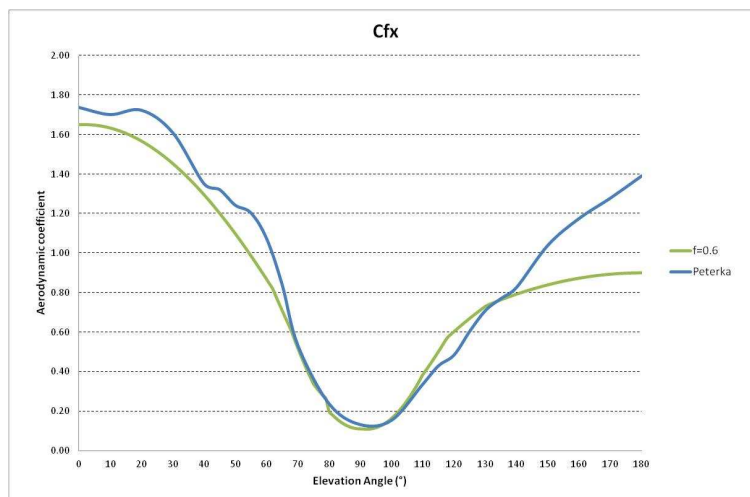


Figure 71 – Comparison of drag force coefficients

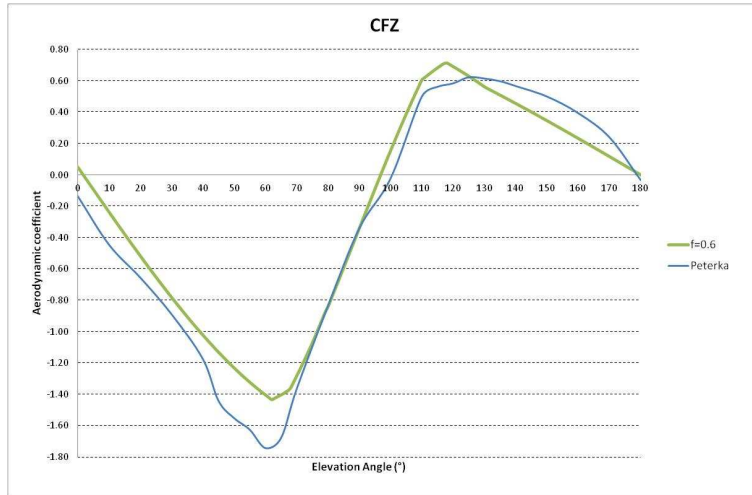


Figure 72 – Comparison of lift force coefficients

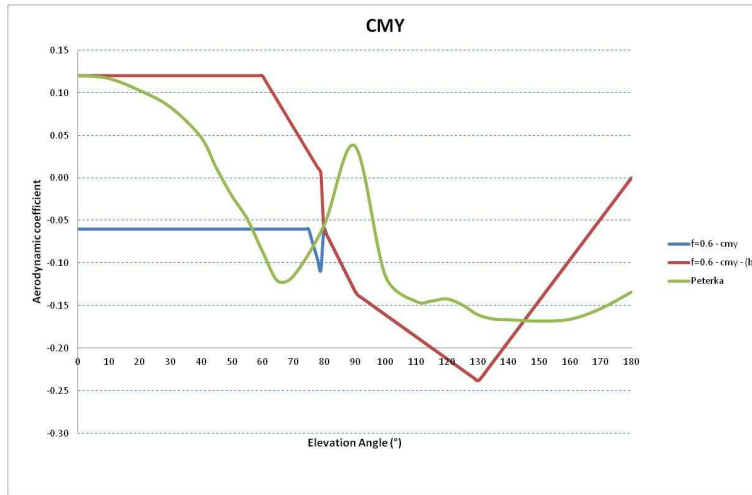


Figure 73 – Comparison of hinge moment coefficients

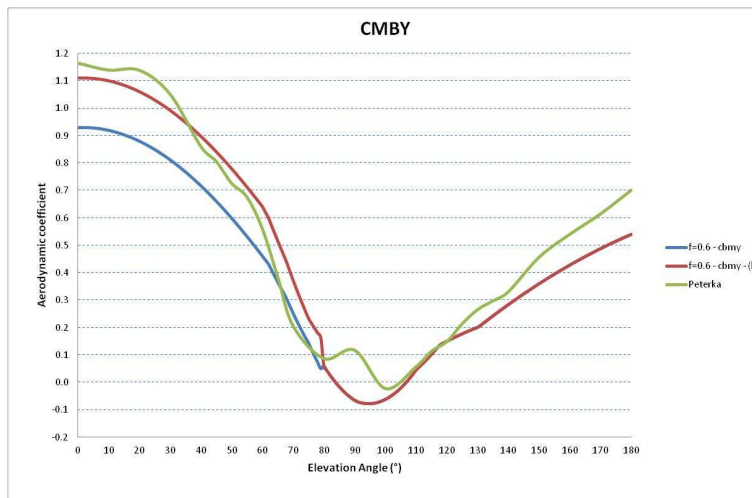


Figure 74 – Comparison of PCD base moment coefficients

From the analysis of the previous figures it is deducible that:

- The trend of drag and lift coefficients as well as the bending moment at the base of the PDC is very similar for both methods. Instead, the trend related to the coefficient of hinge moment shows significant differences;
- The value of the drag coefficient, calculated according to standard, appears to be quite underestimated for elevations angle above 150° . The same evaluation can be made for the PDC base moment.

From the comparison a substantial equivalence between the two methods emerges even if the differences, especially with regards to the evaluation of the moments, cannot be neglected. This could be due to the actual difference between the objects taken into account. The standards refer to parabolic antennas often installed on buildings and subject to a wind with an uniform velocity distribution. Instead, the experimental tests have simulated PDC installed near the ground and exposed to a distribution of wind with increasing speed (logarithmic) from soil. However, it is necessary to emphasize that, even in the case of moments, the maximum aerodynamic coefficients are coincident, and, then, it is still possible to carry out the evaluation of the peak loads due to the wind.

In the following evaluations, the coefficients derived from the experimental tests will be taken into account, in consideration of the fact that the tests were carried out in the same conditions as the Innova prototype.

Characterization of the ENEA Casaccia site

According to the Task2.2, the PDC developed and realized by Innova will be installed at Enea Casaccia site to be tested. The main characteristics of the dish have been listed in Table 6. To evaluate the wind loads acting on the collector, the characteristics of the site must be determined and the maximum wind intensity calculated. The main characteristics of the proposed site are listed below:

Site characteristic	Value	Note
Site name	ENEA Casaccia	
Location	Rome (IT)	
Zone id	3	(tab. 3.I) (*)
Reference speed at sea level (m/s)	27	(tab. 3.I) (*)
Reference altitude (m)	500	(tab. 3.I) (*)
Altitude coefficient	0.37	(tab. 3.I) (*)
Site altitude (m)	100	Casaccia - Rome
Wind return time (y)	50	
Roughness class	C	(tab. 3.III) (*)
Exposition category	II	(fig 3.3) (*)
Exposition parameter (k)	0.19	(tab. 3.II) (*)
Exposition parameter (z_0) (m)	0.05	(tab. 3.II) (*)
Exposition parameter (z_{min}) (m)	4	(tab. 3.II) (*)
Topography coefficient	1	unitary, except special cases (*)
(*) from Italian standards on wind action [4])		

Table 18 – Site data

On the basis of the previous data, it is possible to determine the wind characteristics of the proposed site:

Site characteristic	Value	Note
Altitude coefficient	1	as < a0 (*)
Base reference speed (m/s)	27	
Return coefficient	1	
Project reference speed (m/s)	27	
Wind mean profile coefficient	0.9	
Mean wind speed (m/s)	24.3	
Exposition coefficient	2.0	
Peak wind speed	38.3	
Air mass density (kg/m^3)	1.25	
Peak kinetic pressure (N/m^2)	916.6	
Mean kinetic pressure (N/m^2)	370.3	
(*) from Italian standards on wind action [4]		

Table 19 – Wind speed and Kinetic wind pressure data

Evaluation of the peak forces and moments

The evaluation of the main loads acting on the Innova parabolic dish collector has been performed on the base of the Italian standards and of the above mentioned aerodynamic coefficients. In table 20 a selection of the maximum aerodynamic coefficients for each main wind action is shown.

Maximun aerodynamic coefficients	Azimuth Angle (°)	Elevation Angle (°)	Value
cfx	0	90	1.74
cfy	70	-70	0.27
cfz max	0	-40	0.66
cfz min	0	30	-1.74
cmz	75	-20	-0.145
cmHy max	10	40	0.175
cmHy min	0	25	-0.129

Table 20 – Maximum aerodynamic coefficient

Starting from the previous maximum aerodynamic coefficients and from the peak pressure and the PDC geometrical characteristics (area, diameter) it is possible to evaluate the wind actions using the formulas reported in the previous paragraphs. In the following table the wind loads acting on the PDC rotation point and on the base of the support pylon are shown.

Maximun aerodynamic coefficients	Value
Peak drag force Fx (N)	153399
Peak lateral force Fy (N)	23803
Peak lift force Fz-trac (N)	58186
Peak lift force Fz-comp (N)	-153399
Peak azimuth moment Mz (Nm)	-149948
Peak hinge moment max MHy (Nm)	180972
Peak hinge moment min MHy (Nm)	-133402
<i>On the pylon base ...</i>	
Peak bending y moment My (Nm)	1063019
Peak bending x moment Mx (Nm)	136869
Peak bending moment Mb (Nm)	1071794
Peak torque moment Mt (Nm)	149948
Peak traction force Ft (N)	58186
Peak compression force Fc (N)	153399
Peak shear force T (N)	155235

Table 21 – Peak forces and moments

Conclusions

In this chapter the wind loads acting on the Parabolic Dish Collector proposed by INNOVA for the demo plant have been calculated. The general Italian (and EU) standards have been used to characterize the ENEA Casaccia site. The forces and moments aerodynamic coefficients, as a function of the azimuth and elevation angles, have been extracted by experimental tests in the wind tunnel found in the literature (NREL). Then, selecting the maximum aerodynamic coefficients for each wind action, the main wind loads have been evaluated. These loads will be useful to design/verify the PDC mechanical components and to design the PDC foundation.

Supporting structure

(E. Pastorelli, A. Mariani, (Innova))

From theoretical calculations carried out in collaboration with ENEA, Innova proposes a system with the characteristics listed below, represented in Figure 75:

Design	Aperture diameter	11.73 m
	Focal ratio f/d	0.6
	Geometric con. Ratio	2800
Dish	Design	Stamped sheet metal glued with thin glass
	Panel configuration	Two concentric rings with 27 outer and 13 inner panels
	Reflective surface	Thin glass mirror
	Reflectance	92 %
Structure	Tracking	Azimuth /elevation
	Weight	3000 Kg
Performance	Output thermal	65 kW @ 800 DNI

Table 22 – Summary of PDC characteristics

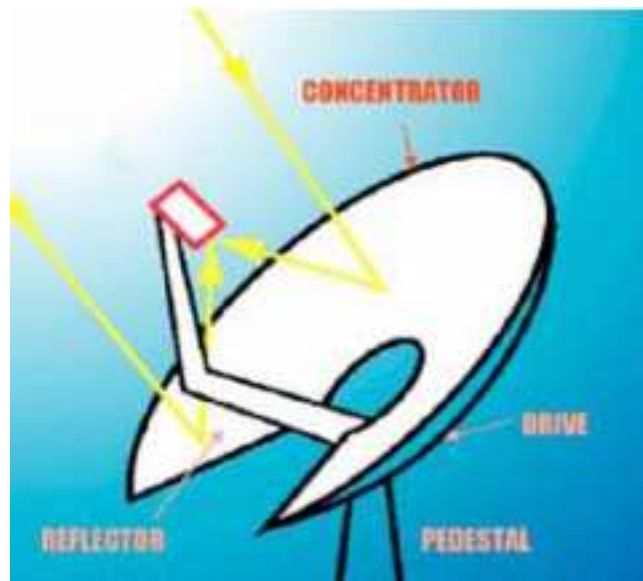


Figure 75: Scheme of the PDC proposed by Innova

The proposed system consists of three macro areas:

- Concentrator and reflector
- Drive
- Pedestal

Concentration and reflector

The choice of the reflecting material (see D1.4) was dictated by a compromise between durability, cost and performance. The dish is composed of two concentric rings, the inner one with 13 reflective panels, the outer with 27 reflective panels (Figure 76).

If ever need the reflective areas can be removed in order to adjust the input power to the turbine.

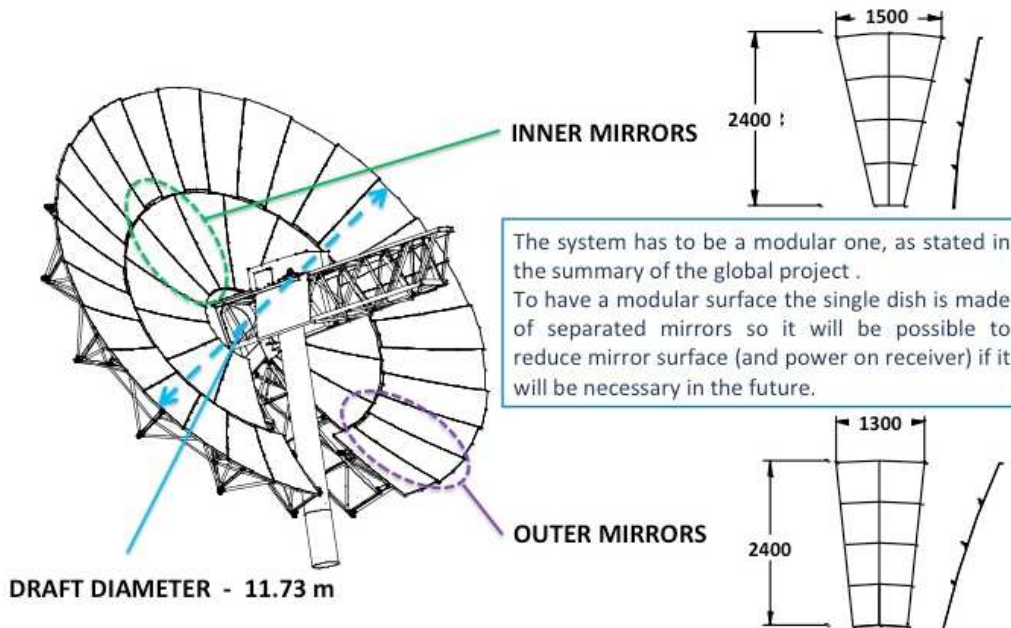


Figure 76 - Structure of the dish

Drive

For handling we have two possible options:

- Slewing drive combined with a planetary gear motor and an electric AC motor with double winding (solution already adopted on Trinum, Figure 77)

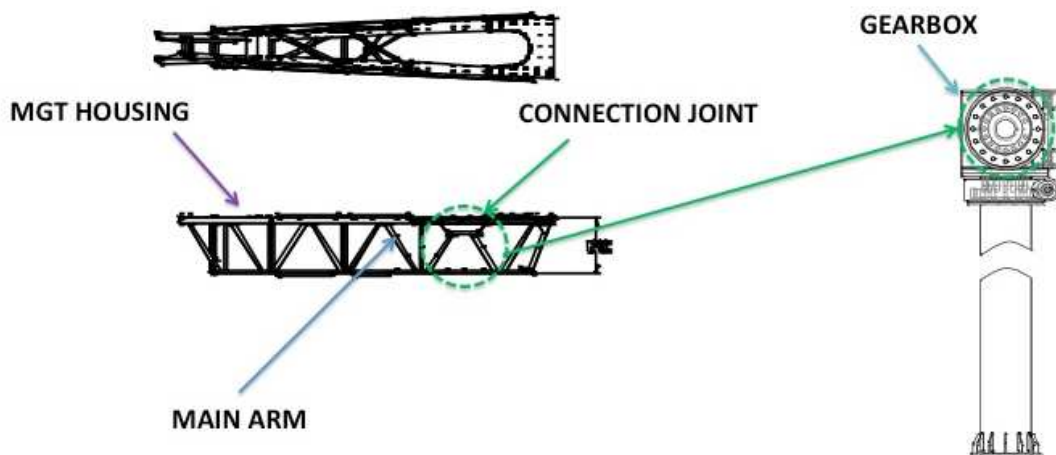


Figure 77: Scheme of the drive

- A new innovative solution that would guarantee the same performance, but with significant improvements in terms of weight, ease of installation cost and consumption of electricity. The movement of the figure below integrate in a single group the two rotations (azimuth, elevation) and related reduction stages, all would be driven by two DC motors.

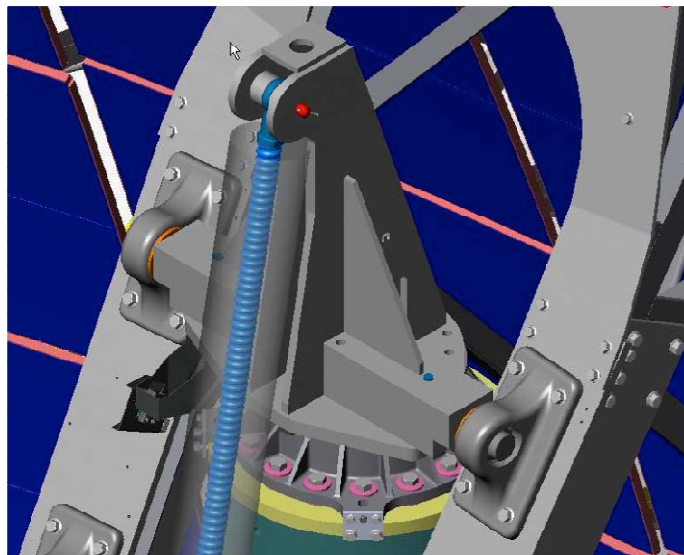


Figure 78: Drive innovative solution

Pedestal

Resulting from the calculation of the wind loads and the conformation of the installation site, it was decided to adopt flanged pole to anchor bolts that come out of the concrete foundation (see figure below).



Figure 79: Pedestal configuration

Tracking system specifications

(E. Pastorelli, A. Mariani (Innova))

SunTrinum is a complete system for the two-axis solar tracking by the astronomical calculation of the equations that govern the motion of the earth relative to the sun.

All information necessary for the operation are detected by an integrated GPS receiver. After the first installation, the system will be completely autonomous since the parameters involved in the operation and configuration of the system are resident in flash memory and protected by a security password.

The interaction of the system with the operator is assigned to a graphic display 128x64 pixels flanked by 5 buttons.

The current SunTrinum unit will be adapted to the new system in terms of hardware (encoder, dc electric motor, wind and rain sensor), and also in the firmware (the firmware will be rewritten to optimize the needs of the machine). The control unit will also be adapted so that it can interact with the control center of ENEA.

Below some particularities of the control unit are reported.

Calculating solar coordinates

The main function of SunTrinum is to calculate the position of the sun (in azimuth and elevation) being known the exact time and terrestrial coordinates of the place of installation.

This information is automatically received by the GPS receiver (Global Positioning System) integrated in KS150, allowing a high degree of automation of the system. Using the GPS , in fact, it is possible to know the exact location of solar tracking system (in terms of latitude, longitude and dial) and the exact time of the astronomical given time.

Based on these parameters the position of the sun on the horizon in terms of azimuth and elevation can be calculated with absolute precision, to ensure effective tracking of the star. The autonomy of the system is completed by a rain and wind sensor, that provide additional details on the meteorological conditions, and consequently, the efficiency of the system.

The tracker turns out to be totally independent in its actions of pointing, and in the ability to assess the overall energy balance.

The calculated values of azimuth and elevation of the sun are shown in real time on the main screen, along with the date and time zone.

Regarding the display of the date and time a parameter is of particular importance: Timezone. It identifies the time zone membership increased by 12 hours. For example, since in Italy the time zone is +1, the value to be entered in parameter is 13.

Operation mode

There are three modes of operation: manual, automatic and safe location.

1) Manual: The system can be set by the operator using the four buttons ▲, ▼, ◀, ▶ (Up, Down, Left, Right). This mode is used during maintenance and to move the dish to taste and to make the first zero of the system;

2) Automatic: The system begins to chase the sun independently, on the base of data calculated by the internal equioment;

3) Safe: The system places the parabola closed down on itself (see parameters AziSafe and ElevSafe) and remains there until the operator decides to put the system back manually or automatically, by pressing the menu. This mode finds its main use in the process of installation and maintenance.

Daily cycle

The system becomes fully operational by setting it in automatic mode. The sleep position is intended to be the configuration of the parabola having azimuth value equal to the value indicated by AziSleep and elevation equal to the value indicated by ElevSleep, expressed in degrees to be considered negative .

The position is reached in the evening, when, considering the position of the sun, the system decides to stop the pursuit and wait for the dawn of the next day.

The safe position is used to bring the dish in security (in case of power failure, wind or rain) and can be set manually by placing the system in safe mode (Menu → Mode → Safe Mode)

The daily cycle begins in the morning, when the system detects that the amount of elevation of the sun is above WakeupElev, expressed in degrees: the parabola comes out from the rest position and from then on begins to chase the sun .

Similarly, during the afternoon, the system returns to the rest position when the height of the sun is lowered below the portion SleepElev, expressed in degrees.

These two parameters are useful to stop the tracking of the sun when this is too close to the horizon in order to provide sufficient energy, in this case the handling would be counterproductive. Refer to the height of the sun rather than to a fixed schedule allows you to have optimal behavior in any season.

For only demonstration purposes, it is possible to simulate the daily movement of the virtual parabola increasing the speed tracking of the sun. The value of the parameter SimulSun indicates the multiplication factor of acceleration of the movement. For example, setting it to 60 per second is equivalent to a real movement of the sun for a minute, then a daily cycle 60 times shorter (the cycle will end in 24 minutes). This parameter must be 0 for the proper functionality of the system.

Conditions external to the system

The system, via sensors, continuously detects the presence of electric network and the possible presence of rain or wind.

Presence of grid. The system is able to detect the presence of electrical network and it can distinguish whether it is powered directly from the grid or via the UPS group. In case of absence of the mains voltage, the parabola will continue to chase the sun for the time indicated by the parameter FltGridOn. After that the system will bring in safe position , not to consume too much battery pending restoration of the network.

Rain sensor. If the sensor detects the presence of rain for a number of seconds at least equal to the value specified by the parameter FltRainOn, the system goes into safe location . After the rain , the system waits for a number of seconds equal to the value specified by the parameter FltRainOff before returning to chase the sun .

Wind speed sensor. If, for a number of seconds at least equal to the value specified by the parameter FltWindOn, it is detected wind speed greater than the value specified by the

parameter MaxWindSpd, expressed in km/h , the system goes into safe position to avoid mechanical damage. Before returning to chase the sun, the system waits for a number of minutes equal to the value specified by the parameter FitWindOff .

References

- [1] *Eurocode 1: Basis of design and actions on structures. Part 2-4: Wind actions*, CEN, ENV 1991-2-4, 1994.
- [2] *Eurocode 1: Actions on structures - General actions. Part 1-4: Wind actions*, CEN, EN 1991- 1-4, 2005.
- [3] *Norme tecniche per le costruzioni*, D.M. 14 Gen 2008.
- [4] *Istruzioni per la valutazione delle azioni e degli effetti del vento sulle costruzioni - CNR-DT 207/2008*
- [5] G. M. Giannuzzi, C. E. Majorana, A. Miliozzi, V.A. Salomoni, D. Nicolini, *Structural Design Criteria for Steel Components of Parabolic-Trough Solar Concentrators*, Jnl of Solar Energy Engineering, Vol. 129 Nov. 2007 pp 382-390
- [6] A. Miliozzi, G.M. Giannuzzi, D. Nicolini, *Valutazione dell'azione del vento su di un concentratore solare parabolico lineare*, ENEA Technical Report RT/TER/13/2007
- [7] F. Crobu, *Analisi numerica e sperimentale dell'azione del vento su concentratori solari parabolici*, Thesis, Perugia University, 2005
- [8] J.A. Peterka, R.G. Derickson, *Wind load design methods for heliostats and parabolic dish collectors*, Sand92-7009, Sep 1992
- [9] J.A. Peterka, R.G. Derickson, J.E. Cermak, *Wind loads and local pressure distributions on parabolic dish collectors*, Seri/TP-253-3668, May 1990
- [10] J.A. Peterka, Z. Tan, B. Bienkiewicz, J.E. Cermak, *Wind loads on heliostats and parabolic dish collectors*, Seri/STR-253-3431, Nov 1988